Cancer Cell

Article

Genetic modeling of *ELP1*-associated Sonic hedgehog medulloblastoma identifies MDM2 as a selective therapeutic target

Graphical abstract

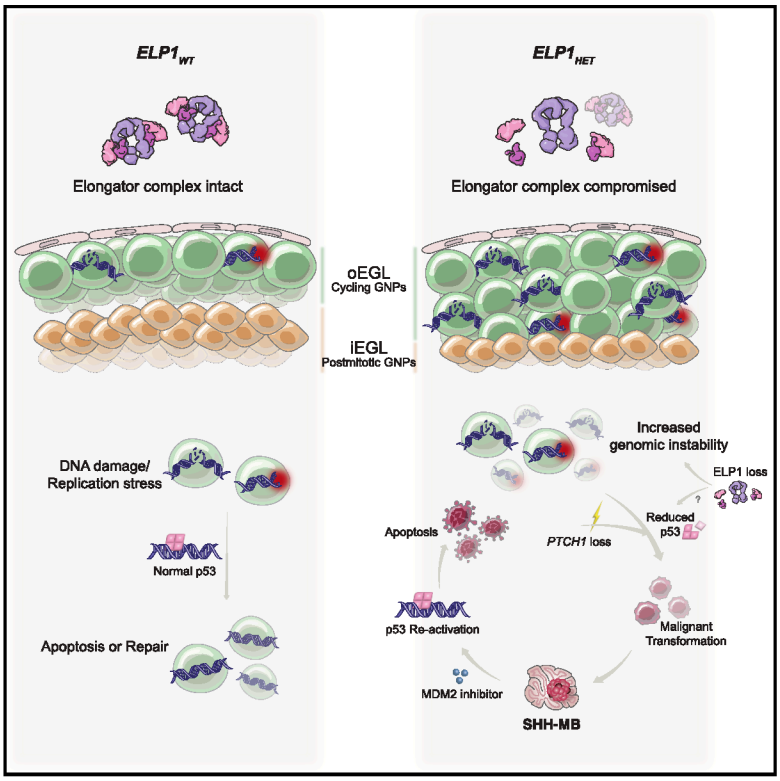

Highlights

- *Elp1*-mutant GNPs exhibit genomic instability, mitotic, and differentiation defects
- *Elp1*-deficient mouse MB recapitulates molecular signatures of human SHH-3 MB
- Reduced p53 signaling renders MDM2 a selective dependency in *ELP1*-mutant SHH-3 MB
- Pharmacological inhibition of MDM2 prolongs survival of *ELP1*-mutant SHH-3 MB

Authors

Shiekh Tanveer Ahmad, Yiran Li, Jesus Garcia-Lopez, ..., Lena M. Kutscher, Hong Lin, Paul A. Northcott

Correspondence

paul.northcott@stjude.org

In brief

Elp1 heterozygous LOF mutations in Sonic hedgehog medulloblastoma (MB) elevate transformation risk in granule neuron precursors through stalled differentiation, DNA replication stress, genomic instability, and accelerated cell cycle. Pharmacological restoration of p53 signaling in *ELP1*-deficient tumor cells suppresses tumor growth and represents a potential therapeutic opportunity.

Ahmad et al., 2025, Cancer Cell *43*, 1141–1158
June 9, 2025
https://doi.org/10.1016/j.ccell.2025.04.014

CellPress

Cancer Cell

CellPress
OPEN ACCESS

Article

Genetic modeling of *ELP1*-associated Sonic hedgehog medulloblastoma identifies MDM2 as a selective therapeutic target

Shiekh Tanveer Ahmad,[1,2,16] Yiran Li,[1,2,16] Jesus Garcia-Lopez,[1,2,16] Brian L. Gudenas,[1,2] Jennifer Hadley,[1,2] Leena Paul,[1,2] Stephanie C. Wu,[1,2] Alaa Refaat,[3] Marija Kojic,[4] Melissa Batts,[1,2] Taha Soliman,[1,2] Aaron Pitre,[5] Frederik Arnskötter,[6] Frederique Zindy,[7] Alun Jones,[8] Nathaniel R. Twarog,[3] Anand Mayasundari,[3] Brandon Bianski,[9] Christopher Tinkle,[9] Abbas Shirinifard,[2] Laura Janke,[10] Meifen Lu,[10] Sara A. Lewis,[1,2] Arzu Onar-Thomas,[11] Stefan M. Pfister,[12] Amar Gajjar,[13] Suzanne J. Baker,[1,2] Martine F. Roussel,[7] Zoran Rankovic,[3] Giles W. Robinson,[13] Brent A. Orr,[10] Brandon Wainwright,[4] Anang A. Shelat,[3] Sebastian M. Waszak,[14,15] Lena M. Kutscher,[6] Hong Lin,[1,2,17] and Paul A. Northcott[1,2,17,18,*]

[1]Center of Excellence in Neuro-Oncology Sciences (CENOS), St. Jude Children's Research Hospital, Memphis, TN 38105, USA
[2]Department of Developmental Neurobiology, St Jude Children's Research Hospital, Memphis, TN 38105, USA
[3]Department of Chemical Biology and Therapeutics, St. Jude Children's Research Hospital, Memphis, TN 38105, USA
[4]Frazer Institute, The University of Queensland, Woolloongabba, QLD 4102, Australia
[5]Cell and Tissue Imaging Shared Resource, St. Jude Children's Research Hospital, Memphis, TN 38105, USA
[6]Hopp Children's Cancer Center Heidelberg (KiTZ), JRG Developmental Origins of Pediatric Cancers, German Cancer Research Center (DKFZ), 69120 Heidelberg, Germany
[7]Department of Tumor Cell Biology, St. Jude Children's Research Hospital, Memphis, TN 38105, USA
[8]Institute for Molecular Bioscience, The University of Queensland, Brisbane, QLD 4102, Australia
[9]Department of Radiation Oncology, St. Jude Children's Research Hospital, Memphis, TN 38105, USA
[10]Department of Pathology, St. Jude Children's Research Hospital, Memphis, TN 38105, USA
[11]Department of Biostatistics, St. Jude Children's Research Hospital, Memphis, TN 38105, USA
[12]Hopp Children's Cancer Center Heidelberg (KiTZ), Division Pediatric Neurooncology, German Cancer Research Center (DKFZ) and German Cancer Consortium (DKTK), Department of Pediatric Hematology and Oncology, Heidelberg University Hospital and National Center for Tumor Diseases (NCT), 69120 Heidelberg, Germany
[13]Department of Oncology, St Jude Children's Research Hospital, Memphis, TN 38105, USA
[14]Swiss Institute for Experimental Cancer Research, School of Life Sciences, École Polytechnique Fédérale de Lausanne (EPFL), CH-1015 Lausanne, Switzerland
[15]Department of Neurology, University of California, San Francisco (UCSF), San Francisco, CA 94143, USA
[16]These authors contributed equally
[17]These authors contributed equally
[18]Lead contact
*Correspondence: paul.northcott@stjude.org
https://doi.org/10.1016/j.ccell.2025.04.014

SUMMARY

Germline loss-of-function (LOF) variants in *Elongator acetyltransferase complex subunit 1 (ELP1)* are the most prevalent predisposing genetic events in childhood medulloblastoma (MB), accounting for ~30% of the Sonic hedgehog (SHH) 3 subtype. The mechanism(s) by which germline *ELP1* deficiency provokes SHH-MB pathogenesis remain unknown. Genetically engineered mice mimicking heterozygous *Elp1* LOF (*Elp1*$_{HET}$) seen in affected germline carriers exhibit hallmark features of premalignancy in cerebellar granule neuron progenitors (GNPs), including increased DNA replication stress, genomic instability, accelerated cell cycle, and stalled differentiation. Orthotopic transplantation of *Elp1*$_{HET}$ GNPs harboring somatic *Ptch1* inactivation yields SHH-MB-like tumors with compromised p53 signaling, providing a plausible explanation for the exclusivity of *ELP1*-associated MBs in the SHH-3 subtype. Preclinical treatment of *ELP1*-mutant patient-derived xenografts with an FDA-approved MDM2 inhibitor reactivates p53-dependent apoptosis and extends survival. Our findings functionally substantiate the role of *ELP1* deficiency in SHH-MB predisposition and nominate therapeutics targeting MDM2 as a rational treatment option.

INTRODUCTION

Sonic hedgehog medulloblastoma (SHH-MB), characterized by hyperactivation of the namesake SHH signaling pathway, accounts for ~30% of all MBs and occurs across all age groups.[1,2] Cerebellar granule neuron progenitors (GNPs) are the developmental origin of SHH-MB, substantiated by genetically engineered mouse (GEM) models and single-cell transcriptomic studies.[3–6] During postnatal cerebellar development, GNPs undergo massive clonal expansion in the outer external granule layer (oEGL), followed by sequential cell cycle exit in the inner EGL (iEGL) and migration to the internal granule layer (IGL) where they function as mature granule neurons (GNs).[7,8] Actively cycling GNPs require rapid and accurate DNA replication, necessitating DNA repair to resolve replication-associated DNA damage.[9] Replication stress occurs when replication fork progression is slowed or stalled, leading to DNA damage normally resolved through intrinsic response mechanisms.[9–13] GNPs harboring extensive and irreparable DNA damage undergo apoptosis, eliminating genomically unstable cells that might be susceptible to malignant transformation.[9] p53 signaling is a critical surveillance pathway that responds to genomic instability by inducing cell cycle arrest, senescence, or apoptosis.[9,14,15]

Germline and somatic *TP53* loss-of-function (LOF) mutations feature prominently in children with SHH-MB and are restricted to the SHH-3 subtype (formerly, SHHα).[16–18] SHH-3 MB patients harboring *TP53* LOF mutations are often refractory to current treatments and considered a high-risk patient group.[16,17] Beyond ~35–40% of SHH-3 MBs harboring *TP53* driver mutations, ~30% of SHH-3 MB is characterized by pathogenic germline variants in *ELP1* that co-occur with somatic *PTCH1* mutations, exhibiting a more favorable outcome.[17–21] *ELP1* encodes the scaffolding subunit of the Elongator complex, a highly conserved multi-protein complex (ELP1 to ELP6) that chemically modifies tRNAs at the U_{34} wobble base position of the anticodon loop (i.e., ncm^5U, mcm^5U, and mcm^5s^2U) to stabilize elongating transcripts.[22,23] Although tissue-specific *ELP1* splicing defects are well characterized in autosomal-recessive familial dysautonomia (FD),[24–32] the mechanisms by which heterozygous germline *ELP1* LOF variants promote SHH-MB are poorly defined. The comparable frequency of *TP53* and *ELP1* mutations observed in SHH-3 MB, coupled with their near-complete mutual exclusivity, provokes the hypothesis that *ELP1* and *TP53* LOF may converge in this subtype, despite notably divergent outcomes.

To determine the biochemical and cellular mechanisms by which germline *ELP1* LOF predisposes children to the development of SHH-3 MB, we generated a novel germline heterozygous LOF *Elp1* mouse model ($Elp1_{HET}$) and performed comprehensive molecular and phenotypic studies. Germline *Elp1* deficiency promoted increased replication stress-associated DNA damage, hyperactive homologous recombination (HR), accelerated cell cycle kinetics, and stalled differentiation of GNPs. Somatic inactivation of *Ptch1* in $Elp1_{HET}$ GNPs resulted in the genesis of SHH-MBs with dampened p53 signaling in an orthotopic transplantation model, and concomitant biallelic inactivation of *Elp1* and *Ptch1* on a p53-deficient background faithfully recapitulated molecular and biochemical signatures of human *ELP1*-associated SHH-MB. Preclinical drug screens in *ELP1*-mutant patient-derived xenograft (PDX) models identified dependency on MDM2 and treatment of PDX-bearing mice with a brain-penetrant MDM2 inhibitor prolonged survival. These studies identify molecular and cellular mechanisms whereby heterozygous *ELP1* mutations likely contribute to the development of SHH-3 MB via stalled GNP differentiation, replication stress-associated genomic instability, and compromised p53 signaling.

RESULTS

Stalled GN lineage differentiation in $Elp1_{HET}$ cerebella

We recently identified *ELP1* as a predisposition gene in ~31% of pediatric SHH-3 MB.[18] To investigate developmental periods of increased tumor risk, we estimated the cumulative risks of SHH-MB based on models incorporating risk ratios, frequencies of SHH-MB, and population incidences of MB, stratified by age (0–4, 5–9, 10–14, 15–19 years).[18,33,34] The prospective UK Biobank cohort (n = 394,841) was used to estimate the population prevalence of rare germline LOF variants in *ELP1* (1 in 1,084 individuals), *PTCH1* (1 in 3,284), *TP53* (1 in 3,401), and *SUFU* (1 in 40,881).[35] During the first two decades of life, the cumulative risk of SHH-MB was estimated to be 0.4% for *ELP1* (95% CI, 0.2%–1.0%), 0.3% (95% CI, 0.1%–1.1%) for *PTCH1*, 0.5% for *TP53* (95% CI, 0.2%–1.8%), and 6.8% for *SUFU* (95% CI, 2.6%–26%) (Figures 1A and S1A; Table S1). While cumulative risk of SHH-MB was similar between *ELP1, PTCH1 and TP53*, the risk was highest during the first decade of life for *ELP1* and until early adolescence for *TP53* (Figure 1A). In contrast, risk of SHH-MB was highest during infancy for *PTCH1* and *SUFU* (Figure S1A). The higher risk for *SUFU* is consistent with pedigree-based studies.[36,37] Collectively, individuals with germline *ELP1, PTCH1* or *TP53* LOF variants exhibit similar risks of developing SHH-MB, motivating in-depth developmental and tumorigenic studies to credential *ELP1* as an SHH-MB driver gene.

To resolve the mechanistic basis of *ELP1*-associated SHH-MB, we generated a germline $Elp1^{+/-}$ mouse model using *CRISPR/Cas9* gene editing (designated as $Elp1_{HET}$ mice) (Figure 1B).[38] Whole-genome sequencing (WGS) confirmed *Elp1*-specific targeting and no off-target effects in other subunits (*Elp2-Elp6*) of the Elongator complex. $Elp1_{HET}$ mice appeared normal in overall appearance and size and did not develop tumors (Figure S1B). Pairwise crossing of $Elp1_{HET}$ mice failed to yield any homozygous $Elp1_{null}$ pups, presumably due to embryonic lethality.[39] Since SHH-MB originates in progenitors of the GN lineage (i.e., GNPs), we studied the molecular and phenotypic consequences of *Elp1* deficiency in GNPs. Bulk RNA sequencing (RNA-seq) analysis confirmed significant reduction of *Elp1* expression in $Elp1_{HET}$ mice compared to $Elp1_{WT}$ mice, but not other subunits (*Elp2-Elp6*), confirming gene targeting specificity (Figure 1C and Table S2). In contrast, tandem mass tag-mass spectrometry (TMT-MS) proteomics revealed significant reduction of ELP1 and other Elongator subunits in $Elp1_{HET}$ GNPs vs. controls (Figure 1D and Table S2). Western blotting validated reduced ELP1 and ELP3 in $Elp1_{HET}$ GNPs (Figure 1E). These results indicate that monoallelic loss of *Elp1* in GNPs likely results in complex destabilization and degradation of other subunits, consistent with studies in other systems.[40]

Failure of GNPs to exit the cell cycle in the EGL increases the likelihood of tumorigenesis, possibly through sustained exposure to pro-proliferative signals.[41–47] We investigated whether germline

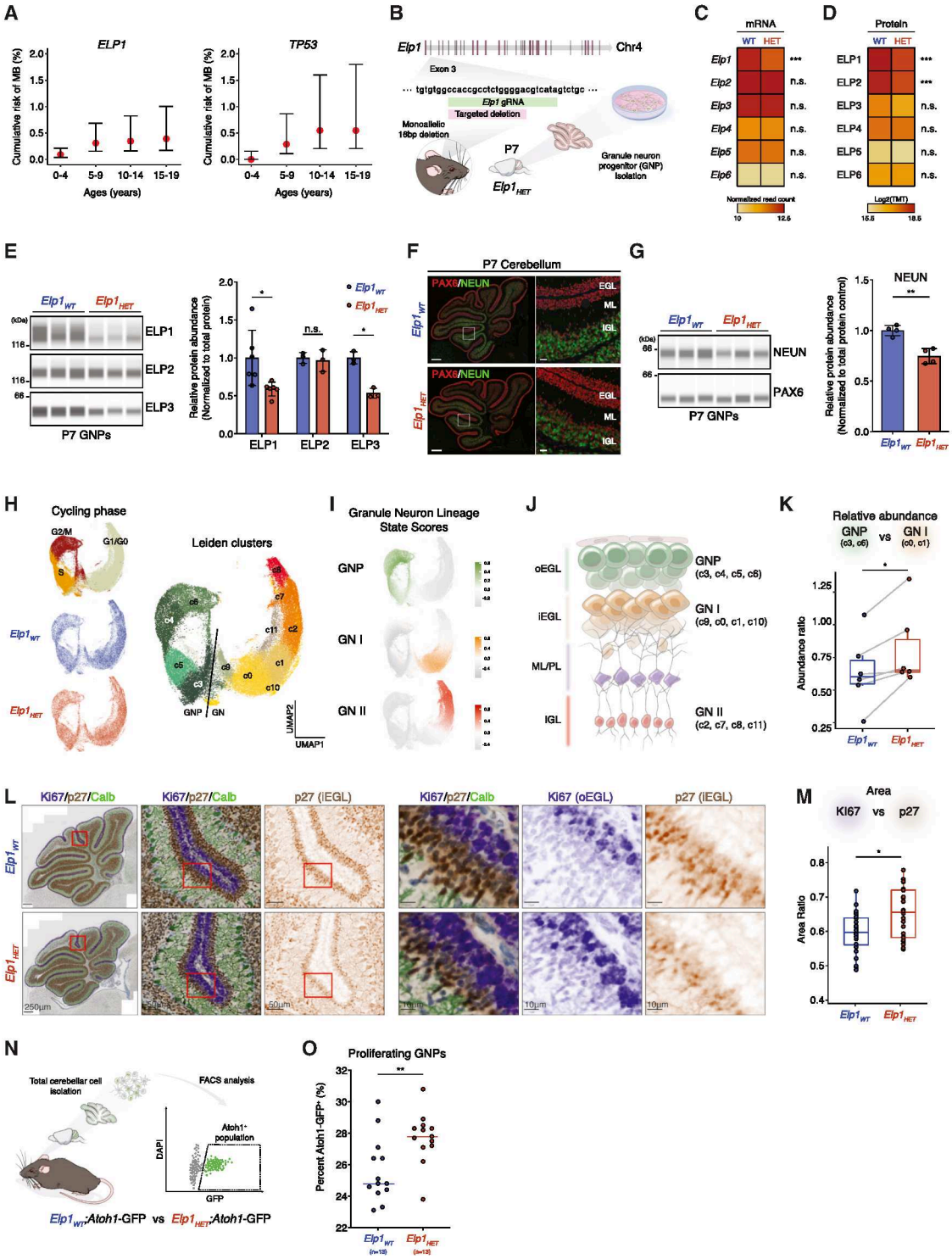

Figure 1. Stalled GN lineage differentiation in *Elp1*$_{HET}$ mouse cerebella

(A) Estimated cumulative risk of SHH-MB for pathogenic *ELP1* and *TP53* germline variants (n = 394,841 individuals).

(B) *Elp1*$_{HET}$ mouse model and GNP isolation from P7 cerebella.

(C and D) RNA (C) and protein (D) expression of Elongator subunits. The data are from 4 independent experiments, each containing GNP cell pellet pooled from 5–10 P7 pups per genotype.

(E) Western blots and quantification of relative ELP1, ELP2, and ELP3 protein abundance normalized to total protein. n = 3 independent experiments. Each experiment contains GNP lysate pooled from 5–10 P7 pups per genotype.

(legend continued on next page)

Elp1 deficiency impacts GN lineage differentiation in the early postnatal mouse cerebellum. In $Elp1_{WT}$ mice, double immunofluorescence imaging revealed high ELP1 expression in Ki67-positive, cycling GNPs of the oEGL (Figure S1C), suggesting that ELP1/Elongator complex might be associated with GNP proliferation and/or differentiation. Hematoxylin-eosin (H&E) staining of P7 $Elp1_{HET}$ vs. $Elp1_{WT}$ cerebellar sections showed no change in the histoarchitecture of cerebellar cortical layers (Figure S1D). However, a marker for mature GNs, NEUN, was significantly decreased by western blot analysis, but not by immunofluorescence. Expression of a GNP marker, PAX6, did not change between $Elp1_{HET}$ vs. $Elp1_{WT}$ cerebella (Figures 1F, 1G, and S1E–S1G).

We investigated the impact of germline *Elp1* deficiency on cellular proportions and differentiation states using scRNA-seq. After quality control filtering, 52,712 cells were analyzed from $Elp1_{HET}$ and $Elp1_{WT}$ cerebella (P7; $n = 8$ donors/genotype), identifying all major cerebellar cell types (Figure S1H). Similar cell type compositions were observed between $Elp1_{HET}$ and $Elp1_{WT}$ cerebella. GNPs and GNs accounted for 80–90% of the dataset (mean 85%) and UMAP clustering yielded a structure where GNPs formed a proliferative loop (*Mki67*$^+$, *Atoh1*$^+$). Postmitotic GNs were marked by *Mapt* and *Rbfox3* (*NeuN*) and could be further subdivided into two cell states, postmitotic precursor (GN I) and mature (GN II) (Figures 1H–1J, S1I, and S1J).[44] Comparing cell state ratios (GNP/GN I; GN I/GN II; GNP/GN II) between paired batches of $Elp1_{HET}$ and $Elp1_{WT}$ mice did not reveal any significant difference (Figure S1K). However, we identified an increase in GNP clusters (C3 and C6) and proportional reduction in GN I clusters (C0 and C1) in $Elp1_{HET}$ cerebella compared to $Elp1_{WT}$ (Figures 1K and S1L).

To validate these findings, we optimized a multiplex chromogen immunohistochemical (IHC) assay to label proliferating GNPs in the oEGL using Ki67, differentiating GNPs in the iEGL (GN I) using p27, and Purkinje neurons using Calbindin (Figure 1L). Proliferating (Ki67$^+$) vs. differentiating (p27$^+$) GNP ratio was increased in $Elp1_{HET}$ mice compared to controls (Figure 1M), despite the increased EGL thickness not reaching statistical significance (Figure S1M). To corroborate these findings, we labeled cycling GNPs by breeding $Elp1_{HET}$ mice with *Atoh1-GFP* reporter mice (Figure 1N)[47] and identified a 12% increase in the proportion of cycling GNPs in $Elp1_{HET}$ vs. $Elp1_{WT}$ mice (Figure 1O).

Complementary analyses indicate that heterozygous germline *Elp1* LOF slows GN lineage differentiation, expanding the pool of actively cycling GNPs and increasing risk of malignant transformation.

Increased DNA replication stress and accelerated cell cycle in $Elp1_{HET}$ GNPs

We analyzed multi-omic signatures in GNPs collected from P7 $Elp1_{HET}$ mice compared to littermate controls. *Elp1* was the only differentially expressed gene by bulk RNA-seq (Figure S2A and Table S2). Given ELP1's crucial role in stabilizing the Elongator complex (essential for efficient translation),[22,23,40] we performed TMT-MS and polysome profiling on isolates from P7 $Elp1_{HET}$ and $Elp1_{WT}$ GNPs. Gene set enrichment analysis (GSEA) of the proteomics data (Tables S2) revealed significant upregulation of DNA replication, replication stress, homologous recombination (HR), homology-directed repair (HDR), and mitochondrial function pathways in $Elp1_{HET}$ GNPs (Figures 2A, 2B, S2B, and Table S2). Examination of leading-edge genes identified DNA replication initiation and elongation processes: MCM Helicase Complex (MCM2-4, MCM7), Origin Recognition Complex (ORC3-6), replication stress response (ATM, ATR, MRN complex) and HDR (RAD51 paralogs, BRCA complex) (Figure 2B). Polysome profiling coupled with RNA-seq analysis confirmed functional enrichment of gene sets associated with DNA replication and ATR activation in response to DNA damage in $Elp1_{HET}$ compared to $Elp1_{WT}$ GNPs (FDR<0.05) (Figures S2C, S2D, and Table S2). Elongator-dependent tRNA modifications (ncm^5U, mcm^5U, and mcm^5s^2U) were unchanged in $Elp1_{HET}$ GNPs (Figure S2E), suggesting residual Elongator complex activity despite the significant reduction in most subunits (Figure 1E). Western blotting of $Elp1_{HET}$ vs. $Elp1_{WT}$ GNP lysates confirmed significant upregulation of MCM2 and *p*-CDK2 (Thr160), unaltered total CDK2 (Figure 2C), and increased activated *p*-CDK2/CDK2 ratio (Figure 2D). CDK2 controls G1/S transition and its hyperactivation promotes S-phase entry and progression, impairs DNA replication, and causes increased replication stress and DNA damage.[48–50] Increased MCM2 levels and CDK2 activity in $Elp1_{HET}$ GNPs are consistent with increased DNA replication and replication stress.

Single-stranded DNA (ssDNA)-bound RPA32 foci significantly increased *in vitro* and *in vivo* in $Elp1_{HET}$ GNPs during S-phase (Figures 2E and S2F). In contrast, total RPA32 protein was

(F) Representative immunofluorescence of PAX6 (red) and NEUN (green). EGL, external granule layer; ML, molecular layer; IGL, internal granule layer. Scale bars – 200 μm for left two panels, 20 μm for right two panels.
(G) Western blots of NEUN and PAX6 and quantification of relative NEUN protein abundance normalized to total protein. $n = 4$ independent experiments. Each experiment contains GNP lysate pooled from 5–10 P7 pups per genotype.
(H) UMAP plots summarizing the GN lineage (GNP and GN populations) annotated by cell cycle (top), genotype (bottom), and Leiden cluster at 0.8 resolution (right) based on transcriptional similarity.
(I) UMAP plots colored by enriched gene sets associated with GNP, GN I, and GN II cell states.
(J) Schematic of cerebellar cortex layers cell state and Leiden clusters. oEGL: outer EGL; iEGL, inner EGL; PL, Purkinje layer.
(K) GNP/GN I cluster ratios of paired samples ($n = 6$ mice per genotype).
(L) Representative IHC images of P10 cerebella showing Ki67$^+$ oEGL (purple), p27$^+$ iEGL (brown) and Calbindin$^+$ ML/PL (green). Scale bars: 250 μm, 50 μm, 50 μm (Left panels) and 10 μm (Right panels).
(M) Quantification of ratio of area in EGL to iEGL in P10 cerebella ($n = 15$ mice for $Elp1_{WT}$ vs. $n = 16$ mice for $Elp1_{HET}$).
(N) Schematic for quantifying cycling GNPs from P7 cerebella.
(O) Cycling GNPs from $Elp1_{HET}$;*Atoh1-GFP* vs. $Elp1_{WT}$;*Atoh1-GFP* ($n = 13$ mice per genotype). Data shown as point estimates ±95% CI (A), mean ± SD (E,G), boxes = median, first, third quartiles whiskers = 1.5x interquartile range (IQR) (K,M), or mean (O). Significance determined using empirical Bayes statistics on linear models adjusted for multiple testing with FDR (C,D), two-sided *t* test (E,G,O), Wilcoxon rank-sum test (K), or Mann-Whitney U-test (M). $^*p < 0.05$, $^{**}p < 0.01$, $^{***}p < 0.001$, n.s. (not significant) $p > 0.05$. See also Figure S1, Tables S1, and S2.

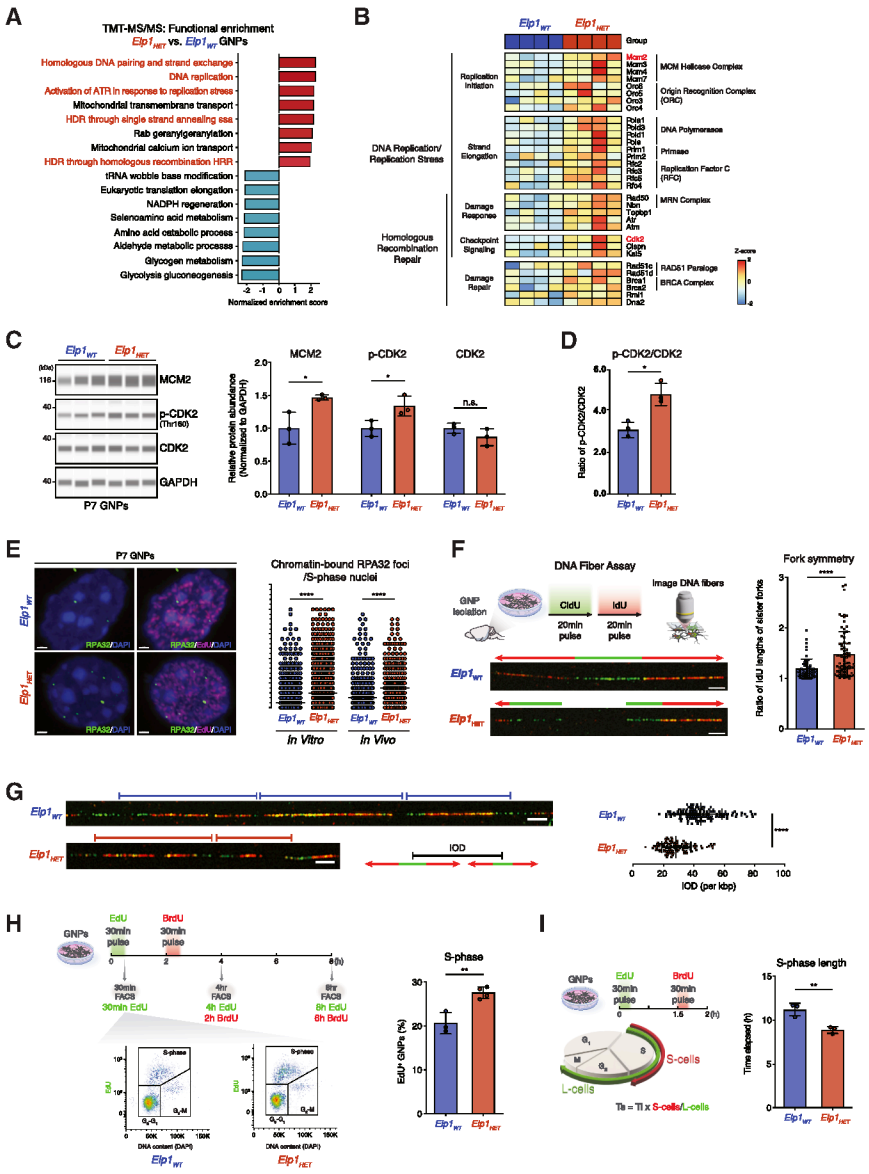

Figure 2. Increased DNA replication stress and accelerated cell cycle kinetics in *Elp1*$_{HET}$ GNPs

(A) Proteomic GSEA of differentially expressed biological processes. Significantly upregulated pathways related to DNA replication stress and HDR in red text.

(B) Heatmap of leading-edge protein expression of gene sets in (A).

(C) Western blot and quantification of relative MCM2, *p*-CDK2, and CDK2 protein abundance normalized to GAPDH. $n = 3$ independent experiments. Each experiment contains GNP lysate pooled from 5–10 P7 pups per genotype.

(D) Quantification of *p*-CDK2/CDK2 ratio from (C). $n = 3$ independent experiments.

(E) Representative immunofluorescence images and quantification of RPA32 foci (green) in EdU-labeled (magenta) S-phase GNPs *in vitro* ($n = 247$ cells for *Elp1*$_{WT}$ vs. $n = 214$ cells for *Elp1*$_{HET}$) and *in vivo* ($n = 702$ cells for *Elp1*$_{WT}$ vs. $n = 1,077$ cells for *Elp1*$_{HET}$). The data are from 3 independent experiments. Scale bars – 1μm.

(F) Schematic of dual CldU/IdU labeling for DNA fiber assay, representative immunofluorescence images and quantification of replication fork symmetry ($n = 61$ sister forks for *Elp1*$_{WT}$ vs. $n = 77$ sister forks for *Elp1*$_{HET}$). The data are from 3 independent experiments. Scale bars – 1μm.

(G) Representative immunofluorescence images, schematic, and quantification of inter-origin distance (IOD) ($n = 121$ neighboring forks for *Elp1*$_{WT}$ vs. $n = 99$ neighboring forks for *Elp1*$_{HET}$). The data are from 3 independent experiments. Scale bars – 2μm.

(H) Schematic for dual EdU/BrdU labeling to track cell cycle dynamics using FACS and quantification of S-phase cells. The data are from $n \geq 3$ independent experiments. Each experiment contains GNPs pooled from 5–10 P7 pups per genotype.

(I) Quantification of S-phase time length. EdU labels L cells that exit the S phase before BrdU labeling, and BrdU labels S cells. Ti represents the time between pulses and Ts is the calculated S-phase speed. $n = 3$ independent experiments. Each experiment contains GNPs pooled from 5–10 P7 pups per genotype. Data shown as mean ± SD (C,D,H,I), median (E) or median±95% CI (F-G). Statistical significance determined by two-sided *t* test (C, D, H, and I) or Mann-Whitney test (E–G). $^{*}p < 0.05$, $^{**}p < 0.01$, $^{****}p < 0.0001$, n.s. $p > 0.05$. See also Figure S2 and Table S2.

reduced in *Elp1*$_{HET}$ vs. *Elp1*$_{WT}$ GNPs (Figure S2G). CDK2 hyperactivation causes aberrant replication origin firing and impaired replication fork progression,[48,49] and depletion of nuclear RPA32 sensitizes nascent ssDNA to DNA double-strand breaks (DSBs) under replication stress.[51] We performed a DNA fiber assay in cultured P7 GNPs as a direct readout of DNA replication stress (Figure 2F). We found significantly increased replication fork asymmetry, decreased inter-origin distance (IOD), (Figures 2F and 2G), and decreased replication fork speed (Figure S2H) in *Elp1*$_{HET}$ vs. *Elp1*$_{WT}$ GNPs. These findings suggest that CDK2 hyperactivation, in the context of germline *Elp1* deficiency, may increase DNA replication stress in GNPs with slowed fork speed, increased replication origin firing, and fork asymmetry.

Increased DNA replication stress influences cell cycle progression fundamental to tumorigenesis.[52,53] To investigate DNA replication stress impact on cell cycle kinetics, *Elp1*$_{HET}$ GNPs were subjected to EdU/BrdU dual labeling (Figure 2H). The initial pulse with EdU for 30 min (min), followed by FACS analysis, revealed significantly more *Elp1*$_{HET}$ GNPs in S-phase (Figure 2H) and fewer in G0-G1 phase compared to controls (Figure S2I), suggesting an augmented transition of *Elp1*$_{HET}$ GNPs from G0-G1 phase to S-phase. GNP progression through cell cycle phases was tracked by EdU/BrdU labeling 2h apart (Figures 2H and S2J). By 4h post-labeling, a higher percentage of *Elp1*$_{HET}$ GNPs transitioned from S-phase through G2/M phases and reached G0/G1 phases (designated as G0*-G1*) than controls (Figure S2K), although most cells remained in S and G2/M phases. The percentage of *Elp1*$_{HET}$ GNPs reaching G0/G1 (G0*-G1*) continued to increase significantly at 6h post-labeling compared to controls (Figure S2L), although the

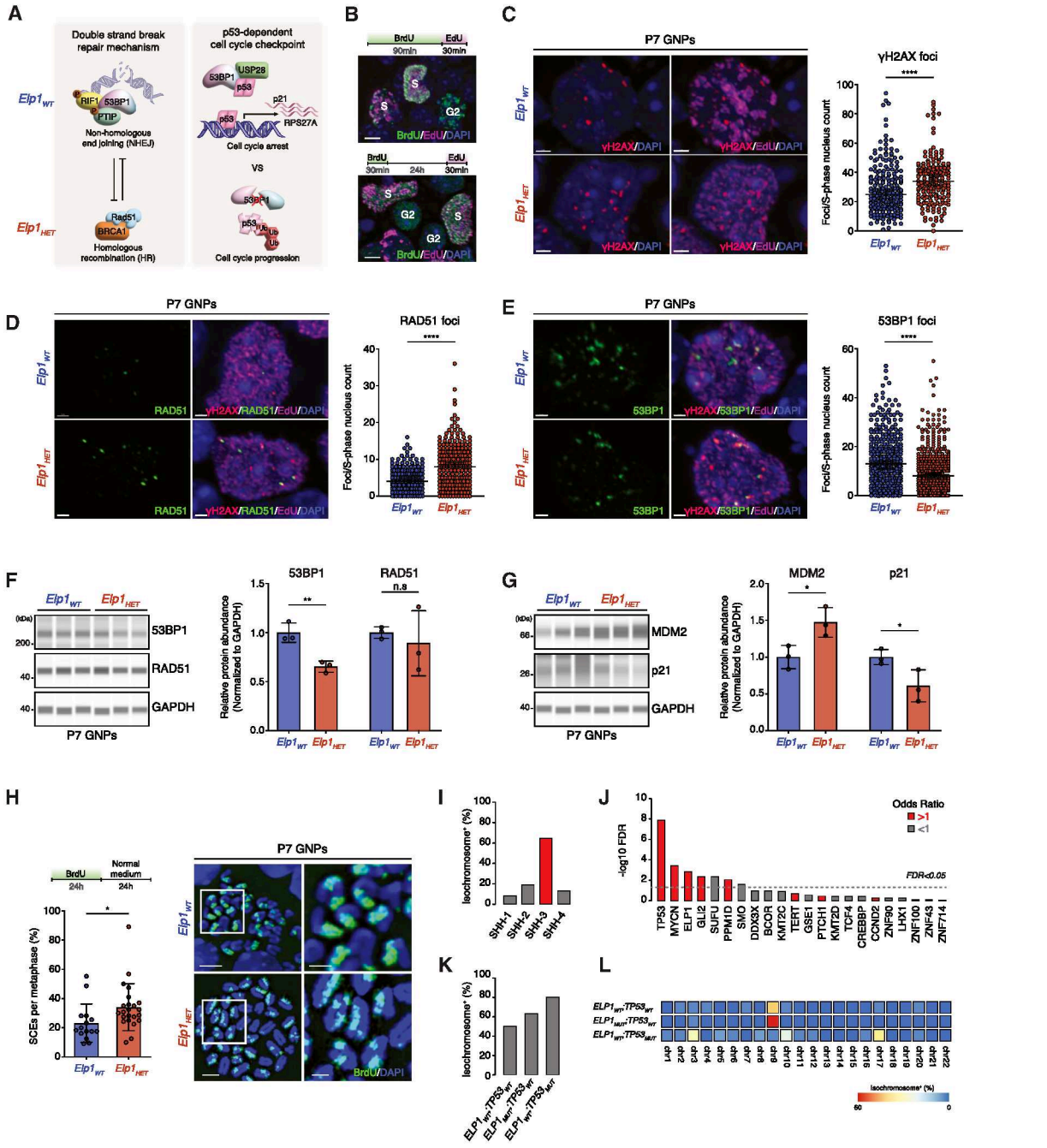

Figure 3. Increased DNA damage/HR repair and compromised p53/53BP1 signaling in *Elp1*$_{HET}$ GNPs

(A) Dual role of 53BP1 in DNA repair pathways and p53-dependent cell cycle checkpoints adapted from.[55]

(B) Labeling strategy for discriminating cell cycle phases in cultured P7 GNPs. Scale bars – 4μm.

(C–E) Representative immunofluorescence images and quantification of DNA damage/repair markers in EdU^{+} labeled S-phase GNPs (magenta). Scale bars – 2μm. $n = 3$ independent experiments. Each experiment contains GNPs pooled from 5–10 P7 pups per genotype. (C) γH2AX foci (red) ($n = 215$ cells for *Elp1*$_{WT}$ vs. $n = 176$ cells for *Elp1*$_{HET}$). (D) RAD51 foci (green) ($n = 182$ cells for *Elp1*$_{WT}$ vs. $n = 222$ cells for *Elp1*$_{HET}$). (E) 53BP1 foci (green) ($n = 385$ cells for *Elp1*$_{WT}$ vs. $n = 401$ cells for *Elp1*$_{HET}$).

(F and G) Western blots and quantification of relative (F) 53BP1 and RAD51 and (G) MDM2 and p21 protein abundance normalized to GAPDH. $n = 3$ independent experiments. Each experiment contains GNP lysate pooled from 5–10 P7 pups per genotype.

(H) Quantification of sister chromatid exchange (SCE) per metaphase ($n = 15$ metaphases for *Elp1*$_{WT}$ vs. $n = 24$ metaphases for *Elp1*$_{HET}$). Scale bar for left panel – 5 μm and right panel – 1μm. The data are from 3 independent experiments.

(I) Frequency of somatic isochromosome events by SHH-MB subtype ($n = 137$ individuals).

(legend continued on next page)

difference was not significant at 8h post-labeling (Figure S2M). EdU/BrdU dual labeling for estimation of S-Phase time[54] identified a 35% reduction (mean S-phase 7.1h for $Elp1_{HET}$ and 10.9h for $Elp1_{WT}$; Figure 2I). Overall, this indicates that *Elp1* germline deficiency intensifies replication stress and accelerates S-phase in cycling GNPs.

Increased DNA damage and compromised p53 signaling in $Elp1_{HET}$ GNPs

DNA replication stress leads to DNA damage, triggering p53/53BP1 signaling to maintain replication fork integrity, activate HDR or non-homologous end-joining (NHEJ) DNA repair, and regulate cell cycle checkpoints (Figure 3A).[55–61] We investigated susceptibility to DNA damage across cell cycle phases (Figure 3B). During S-phase, $Elp1_{HET}$ GNPs had significantly increased γ-H2AX foci compared to controls (Figure 3C). $Elp1_{HET}$ γ-H2AX foci remained elevated during G2 and G0/G1 phases (Figures S3A and S3B) with the highest frequency during S-phase (Figure 3C). *In vivo* studies in $Elp1_{HET}$ vs. $Elp1_{WT}$ mice at P7 (Figure S3C) substantiated germline *Elp1* deficiency promotes DNA DSBs during S-phase.

Proliferative cells preferentially resolve DNA damage arising from replication stress by HR repair.[62] RAD51 is a core component of the HR repair pathway,[63] and 53BP1 promotes NHEJ by blocking HR (Figure 3A).[64] RAD51 foci significantly increased in S-phase $Elp1_{HET}$ GNPs *in vitro* (Figure 3D) and *in vivo* (Figure S3D). Conversely, 53BP1 foci decreased in $Elp1_{HET}$ GNPs during S-phase, but not other cell cycle phases (Figures 3E and S3E). Western blotting confirmed reduced 53BP1 in $Elp1_{HET}$ GNPs, whereas RAD51 levels were comparable with controls (Figure 3F). We examined p53 signaling by assessing protein levels of p53, MDM2 (a negative regulator of p53), cleaved caspase-3 (CC3, a downstream target of p53-mediated apoptosis), and p21 (a transcriptional target of p53-mediated cell cycle arrest). Basal p53 protein levels trended downward (n.s.) in $Elp1_{HET}$ vs. $Elp1_{WT}$ GNP lysates by Western blotting, and minimal nuclear p53 was detected by IHC in P7 EGL of both genotypes (Figures S3F–S3H). Basal CC3 protein levels were not detectable by Western blotting or IHC in either genotype (Figures S3F and S3H). However, MDM2 significantly increased and p21 significantly decreased in $Elp1_{HET}$ vs. $Elp1_{WT}$ GNPs (Figure 3G). To assess the consequences of DNA replication stress and hyperactive HR repair in $Elp1_{HET}$ GNPs, we evaluated sister chromatid exchange (SCE) DNA recombination events during mitosis.[65] $Elp1_{HET}$ GNPs had significantly increased SCE events compared to controls, suggesting that hyper-recombination with *Elp1* deficiency may predispose GNPs to genomic instability (Figure 3H).

We previously observed higher rates of isochromosome 9p formation in *ELP1*-mutant SHH-MB.[18] Re-analysis of human SHH-MB genomes demonstrated that isochromosome 9p is among the most frequent cytogenetic events in this subgroup (Figures S3I, S3J, and Table S1), occurring more frequently in SHH-3 MB compared to other SHH-MB subtypes (65% vs. 8–19%) (Figure 3I). Isochromosomes occur more frequently in SHH-MBs harboring driver gene alterations in *TP53*, *ELP1,* and *PPM1D* (FDR<0.05) (Figure 3J). Significantly more *ELP1*-mutant (62%) and *TP53*-mutant (80%) SHH-3 MBs had somatic isochromosome events (Figure 3K) than $ELP1_{WT};TP53_{WT}$ SHH-3 MBs (∼50%; *p*-value = 0.04, Chi-square test). The most frequent isochromosome events in *ELP1*-mutant and *TP53*-mutant MBs involved chromosome 9 and chromosomes 3, 10, and 17, respectively (Figure 3L). Overall, these data suggest that p53 dysregulation via somatic/germline *TP53* mutations, somatic *PPM1D* alterations, or germline *ELP1* variants contributes to isochromosome formation events in SHH-3 MB. These data are consistent with pan-cancer studies and increased rates of HR and isochromosome events in *TP53*-altered tumors.[66]

Collectively, these results indicate that germline *Elp1* deficiency compromises p53/53BP1 signaling in $Elp1_{HET}$ GNPs, contributing to hyperactive HR and genomic instability.

Generation and characterization of *Elp1*-deficient SHH-MB models

To evaluate the tumorigenic potential of germline *Elp1* deficiency using an orthotopic transplantation model, GNPs were isolated from *Cas9-GFP;*$Elp1_{HET}$ and *Cas9-GFP;*$Elp1_{WT}$ littermates, transduced with gRNA-carrying lentivirus targeting the SHH-3 MB driver *Ptch1*, and implanted into the cerebella of immunocompromised mice (Figure 4A). Comparable *Ptch1* editing efficiency was confirmed by sequencing (Figure S4A). Surprisingly, mice implanted with $Elp1_{WT};Ptch1_{gRNA}$ GNPs developed tumors with increased penetrance (22/32; 69%) compared with $Elp1_{HET};Ptch1_{gRNA}$ GNP recipients (18/40; 45%) (Figure S4B). However, we observed no difference in overall survival and latency between mice bearing $Elp1_{WT};Ptch1_{gRNA}$ and $Elp1_{HET};Ptch1_{gRNA}$ tumors (Figure 4B). Histopathological evaluation of resulting tumors revealed a small cell embryonal phenotype with no significant anaplasia. IHC confirmed strong, diffuse expression of the SHH-MB specific marker, GAB1, and cytoplasmic expression of β-catenin, resembling the clinicopathological phenotypes of human *ELP1-wildtype* and *ELP1-mutant* SHH-MB[68] (Figure 4C). Notably, YAP1 immunoreactivity was relatively low in both mouse tumor models compared to human SHH-MB tumors (Figure 4C), consistent with YAP1 staining in a *Ptch1* LOF model.[69] Western blotting revealed a significant reduction of ELP1 and ELP3, with no change in ELP2 expression in $Elp1_{HET};Ptch1_{gRNA}$ tumors compared to controls (Figure 4D). Unsupervised UMAP clustering of DNA methylation and transcriptome profiles confirmed similarity of both mouse models to human SHH-MB patient tumors (Figures 4E and S4C). Transcriptomic analysis revealed significantly downregulated p53 signaling and DNA repair and upregulated mitochondrial metabolism pathways in $Elp1_{HET};Ptch1_{gRNA}$ vs. $Elp1_{WT};Ptch1g_{RNA}$

(J) Association between somatic/germline gene mutations and isochromosome events in SHH-MB. OR>1 indicates higher odds, OR<1 indicates lower odds of isochromosomes in SHH-MBs with somatic/germline gene mutations. *p* values were calculated for each gene and corrected for multiple testing using the Benjamini-Hochberg method to control FDR.

(K) Somatic isochromosomes in SHH-3 MB (*n* = 85 individuals) stratified by somatic/germline driver mutations in *ELP1* and *TP53*.

(L) Chromosomal distribution of somatic isochromosomes in SHH-3 MB (*n* = 85 individuals). Data shown as median±95%CI (C–E) or mean ± SD (F–H). Statistical significance determined by Mann-Whitney test (C–E) or two-sided *t* test (F–H). $^{*}p < 0.05$, $^{**}p < 0.01$, $^{****}p < 0.0001$, n.s. $p > 0.05$. See also Figure S3 and Table S1.

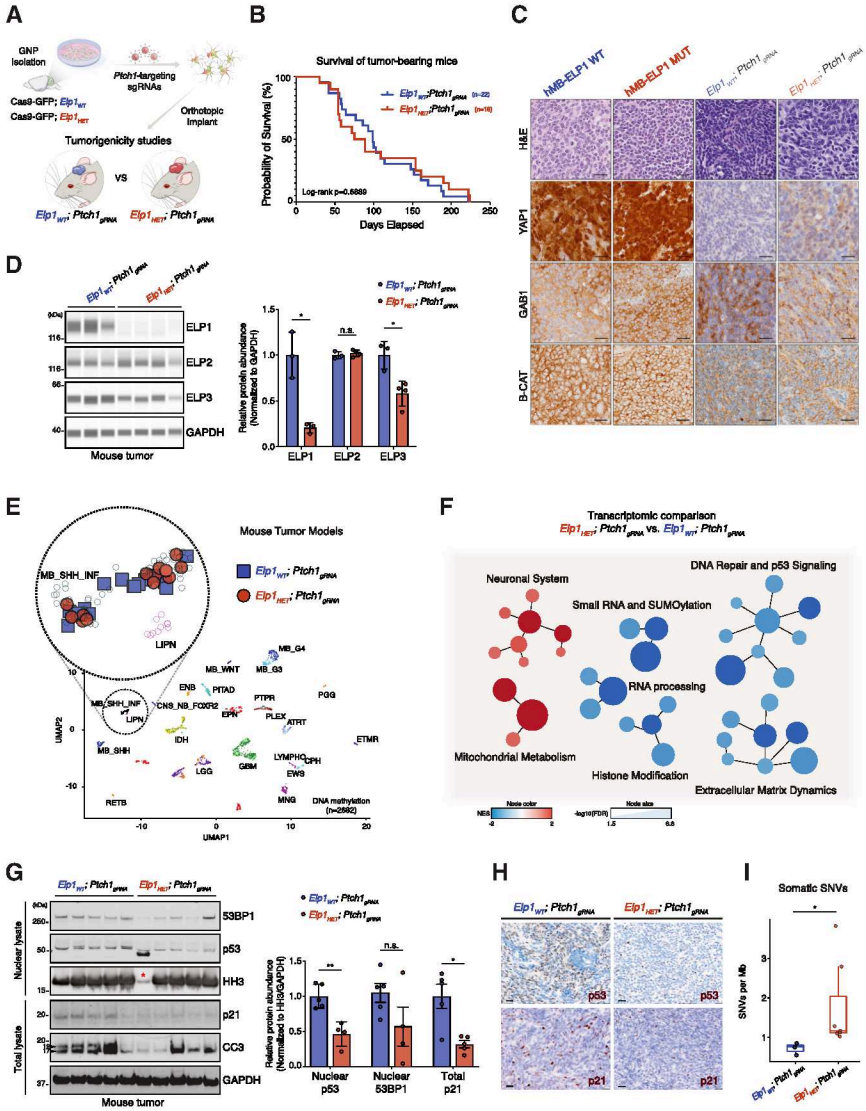

Figure 4. *Elp1*$_{HET}$;*Ptch1*-targeted SHH-MB models with dampened p53 signaling

(A) Schematic of *Elp1*$_{HET}$;*Ptch1*$_{gRNA}$ and *Elp1*$_{WT}$;*Ptch1*$_{gRNA}$ orthotopic implant MB models.

(B) Survival curves of tumor-bearing mice implanted with *Elp1*$_{WT}$;*Ptch1*$_{gRNA}$ (n = 22 mice) vs. *Elp1*$_{HET}$;*Ptch1*$_{gRNA}$ (n = 18 mice) GNPs after tumor onset detected by MRI.

(C) Human *ELP1-WT* and *ELP1-mutant* SHH-MB tumors and mouse *Elp1*$_{WT}$;*Ptch1*$_{gRNA}$ and *Elp1*$_{HET}$;*Ptch1*$_{gRNA}$ tumors stained with H&E, YAP1, GAB1, and β-Catenin (B-CAT). Scale bars – 50μm.

(D) Western blots and quantification of relative ELP1, ELP2, and ELP3 protein abundance normalized to GAPDH (n = 4 for *Elp1*$_{HET}$;*Ptch1*$_{gRNA}$ vs. n = 3 for *Elp1*$_{WT}$;*Ptch1*$_{gRNA}$ tumors).

(E) Unsupervised clustering of reference human CNS tumor methylation profiles[67] and mouse models using the top 4,000 shared variable probes. Closely aligned mouse and human CNS tumors are circled.

(F) Network visualization of GSEA transcriptome comparison. Nodes symbolize gene sets, shaded according to the Normalized Enrichment Score (NES) and scaled based on enrichment significance. Edges representing a shared leading-edge subset >25%. Major biological processes annotated for each cluster (n = 13 for *Elp1*$_{HET}$;*Ptch1*$_{gRNA}$ vs. n = 17 for *Elp1*$_{WT}$;*Ptch1*$_{gRNA}$ tumors).

(G) Western blots of p53, 53BP1, p21 and cleaved caspase-3, and quantification of relative p53, 53BP1 protein abundance normalized to Histone H3 in the nuclear fraction and p21 normalized to GAPDH in whole-cell lysate of tumors ($n \geq 4$ tumors per genotype). * Nuclear isolation failed in this sample.

(H) Representative IHC images of p53 and p21 expression in *Elp1*$_{HET}$;*Ptch1*$_{gRNA}$ vs. *Elp1*$_{WT}$;*Ptch1*$_{gRNA}$ tumors. Scale bars – 25μm.

(I) Boxplot of somatic tumor SNV mutation frequencies. (n = 3 *Elp1*$_{WT}$;*Ptch1*$_{gRNA}$ vs. n = 7 *Elp1*$_{HET}$;*Ptch1*$_{gRNA}$ tumors). Data shown as mean ± SD (D), mean ± SEM (G), or boxes = median, first and third quartiles, whiskers = 1.5x IQR (I). Statistical significance determined by Log rank Mantel-Cox test (B), two-sided t test (D and G), or Mann-Whitney test (i). *$p < 0.05$, **$p < 0.01$, n.s. $p > 0.05$. See also Figure S4 and Table S3.

tumors (Figure 4F and Table S3). Increased mitochondrial metabolism may reflect higher energy demands during DNA replication in cycling cells[70,71] and/or replication stress[72] in the context of *Elp1*$_{HET}$ deficiency.

In normal cells, p53 is expressed at low levels in an inactive form. In response to stress, p53 is activated and stabilized in the nucleus.[73–75] To investigate the p53 pathway in *Elp1*$_{HET}$;*Ptch1*$_{gRNA}$ tumors, we assessed protein levels of p53, 53BP1, p21, CC3, MDM2, and RPS27a. p53, p21 and the 19 kDa isoform of CC3 were significantly reduced in *Elp1*$_{HET}$;*Ptch1*$_{gRNA}$ tumors (Figures 4G and S4D–S4F), whereas a reduction in 53BP1 did not reach statistical significance (Figure 4G). The p53-pathway regulator RPS27a was significantly downregulated, with no change in MDM2 (Figures S4G–S4I). IHC staining confirmed p53, p21, and CC3 downregulation (Figures 4H and S4J–S4L). These results suggest *ELP1* deficiency dampens p53-mediated cell cycle checkpoint signaling, potentially allowing GNPs to evade cell cycle arrest/apoptosis. As 100% of *ELP1*-associated SHH-MB patient tumors exhibit biallelic inactivation,[18] *Elp1*$_{HET}$;*Ptch1*$_{gRNA}$ tumors were also evaluated for biallelic inactivation. Although ELP1 protein expression was reduced by ~70–80% compared to controls (Figure 4D), we did not find evidence of biallelic inactivation of the *Elp1* gene at the genetic or transcriptional level in *Elp1*$_{HET}$;*Ptch1*$_{gRNA}$ tumors (Figure S4M). Genome-wide mutational analysis revealed significantly increased somatic single nucleotide variants (SNVs) in *Elp1*$_{HET}$;*Ptch1*$_{gRNA}$ tumors (Figure 4I), strengthening the proposed link between germline *ELP1* deficiency and genomic instability. Together, *Elp1*$_{HET}$;*Ptch1*$_{gRNA}$ tumors exhibit histological and molecular features of SHH-3 MB and

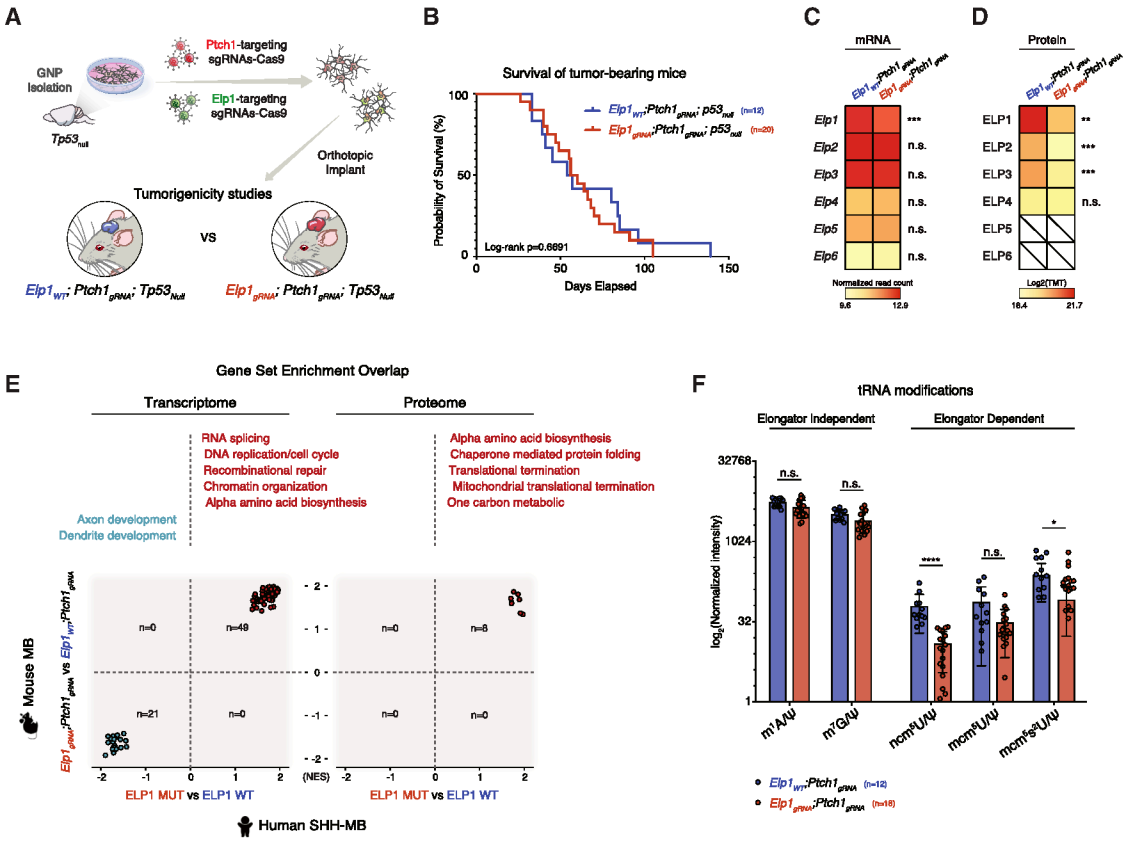

Figure 5. Dual-targeting *Elp1* and *Ptch1* in $p53_{null}$ GNPs recapitulates SHH-MB patient tumor features

(A) Targeting *Ptch1* and *Elp1* in $p53_{Null}$ GNPs to generate $Elp1_{WT}$;$Ptch1_{gRNA}$;$p53_{null}$ and $Elp1_{gRNA}$;$Ptch1_{gRNA}$;$p53_{null}$ MB models.

(B) Survival curves of mice implanted with $Elp1_{gRNA}$;$Ptch1_{gRNA}$;$p53_{null}$ (n = 20) vs. $Elp1_{WT}$;$Ptch1_{gRNA}$;$p53_{null}$ (n = 12) GNPs after tumor onset detected by MRI.

(C and D) RNA (C) and protein (D) expression of Elongator subunits in $Elp1_{gRNA}$;$Ptch1_{gRNA}$;$p53_{Null}$ and $Elp1_{WT}$;$Ptch1_{gRNA}$;$p53_{null}$ mouse tumors (For RNA n = 8 and protein n = 6 for $Elp1_{WT}$;$Ptch1_{gRNA}$;$p53_{null}$ and for RNA n = 15 and protein n = 8 for $Elp1_{gRNA}$;$Ptch1_{gRNA}$;$p53_{Null}$).

(E) GSEA analysis of $Elp1_{gRNA}$;$Ptch1_{gRNA}$;$P53_{null}$ tumor similarity to human *ELP1-mutant* SHH-MB. Transcriptomic signatures share 49 upregulated and 21 downregulated gene ontology (GO) terms. Proteomic signatures share 8 upregulated gene sets between $Elp1_{gRNA}$;$Ptch1_{gRNA}$;$p53_{null}$ vs. $Elp1_{WT}$;$Ptch1_{gRNA}$;$p53_{null}$ mouse tumors and human *ELP1*-mutant vs. *ELP-WT* SHH-MB. NES, Normalized Enrichment Score.

(F) Quantification of Elongator-dependent and -independent tRNA-modifications in lysates collected from $Elp1_{gRNA}$;$Ptch1_{gRNA}$;$p53_{null}$ (n = 18) and $Elp1_{WT}$;$Ptch1_{gRNA}$;$p53_{null}$ (n = 12) tumors. Data shown as mean ± SD (F). Statistical significance calculated by Log rank Mantel-Cox test (B), empirical Bayes statistics on linear models adjusted for multiple testing with FDR (C,D), or two-sided t test (F). $^{*}p < 0.05$, $^{**}p < 0.01$, $^{***}p < 0.0001$, n.s. $p > 0.05$. See also Figure S5, Tables S4 and S5.

implicate compromised p53 signaling in *ELP1*-associated SHH-3 MB etiology.

We recapitulated biallelic inactivation of *ELP1* characteristic of SHH-MB patient tumors with *CRISPR/Cas9* gene editing concomitantly targeting both *Elp1* and *Ptch1* in GNPs prior to implantation into the cerebella of immunodeficient mice. Surprisingly, mice implanted with dually targeted $Elp1_{gRNA}$;$Ptch1_{gRNA}$ GNPs failed to develop tumors (0/9 $Ptch1_{gRNA}$;$Elp1_{gRNA}$ GNP implants). To investigate the fate of transduced GNPs, we performed bulk RNA-seq of cells 36h and 72h post-transduction. At 36h, DNA damage repair pathways were downregulated, followed by activation of p53-dependent apoptotic signaling at 72h (Figures S5A, S5B and Table S4). These results indicate biallelic *Elp1* loss activates apoptosis in GNPs, explaining the lack of tumorigenesis in implanted mice, consistent with *ELP1* essentiality in other cell types.[24,76] Somatic targeting of the remaining *Elp1* allele in $Elp1_{HET}$;$Ptch1_{gRNA}$ tumors did not trigger apoptosis and implanted mice still developed tumors (Figure S5C). These findings suggest ELP1 is essential for GNP survival during development but not in the malignant setting.

To circumvent p53-dependent apoptosis consequent to biallelic *Elp1* inactivation, GNPs from $p53_{null}$ mice were subjected to *CRISPR/Cas9* gene editing to inactivate both *Elp1* and *Ptch1* or *Ptch1* alone and implanted for tumorigenic studies (Figure 5A). Transduced GNPs from both groups developed tumors with 100% penetrance with no difference in survival (Figure 5B). *Ptch1* and *Elp1* editing efficiency was confirmed by sequencing (Figure S5D). Transcriptomic analysis of tumors confirmed a significant reduction of *Elp1*, but not other subunits (*Elp2-Elp6*), confirming gene targeting specificity (Figure 5C). Proteomics revealed a significant reduction of ELP1, ELP2, and ELP3 (Figure 5D), substantiating destabilization of the core Elongator complex. DNA methylation analysis confirmed similarity of both models to SHH-MB (Figure S5E). $Elp1_{gRNA}$;$Ptch1_{gRNA}$;$p53_{null}$ tumors were

molecularly distinct from *Elp1*$_{WT}$;*Ptch1*$_{gRNA}$;*p53*$_{null}$ tumors (Figures S5F, S5G, and Table S5). Transcriptionally, biological processes associated with DNA replication, HDR, and additional pathways were concordantly upregulated in *Elp1*-associated mouse tumors and *ELP1*-mutant SHH-MB patient tumors, while neuronal developmental processes were downregulated (Figure 5E and Table S5). At the proteome level, gene sets associated with translational termination, protein folding, and alpha amino acid biosynthesis were upregulated in *Elp1*-associated mouse tumors and SHH-MB patient tumors (Figure 5E and Table S5). HPLC and MS/MS confirmed a significant reduction in Elongator-dependent tRNA modifications (ncm^{5}U and mcm^{5}s^{2}U) in *Elp1*$_{gRNA}$;*Ptch1*$_{gRNA}$;*p53*$_{null}$ tumors, but not Elongator-independent modifications (m^{1}A and m^{7}G) (Figure 5F), consistent with *ELP1*-associated SHH-MB patient tumors.[18] Hence, the molecular, biological, and biochemical defects observed in *Elp1* deficient SHH-MB models recapitulate core phenotypes observed in human *ELP1*-associated SHH-MBs.

Sensitivity of *ELP1*-mutant SHH-MB models to MDM2 inhibition

To expose therapeutic vulnerabilities of *ELP1*-associated SHH-MB, we performed preclinical drug screening on five SHH-MB PDX lines including two verified *ELP1-mutant* models, MED1712FH and RCMB24; one *ELP1-wildtype (WT)* model, MED113FH; and two *TP53-mutant* SHH models, SJMBSHH-13-5634 (*TP53:p.T125R and MYCN* amplification) and SJMBSHH-14-7196 (*TP53:p.A138P* and *PTCH1*/9q loss) with an FDA-approved compound library (Figure S6A and Table S6).[77,78] We identified RG7388 (idasanutlin), a potent blood-brain barrier (BBB)-penetrant second-generation MDM2 inhibitor,[79,80] and PF-03758309, a PAK4 (p21-activated kinase) inhibitor as selective for *ELP1-mutant* SHH-MB PDX (Figures 6A and S6A). Since PF-03758309 failed in Phase I clinical trials[81,82] and p53 pathway suppression was observed across our mouse models, we investigated the preclinical efficacy of idasanutlin. Exposure to idasanutlin potently induced cell death in both *ELP1-mutant* PDX lines (IC50 < 0.3μM), but not in *ELP1-wildtype* or *TP53-mutant* lines (IC50 > 10μM) (Figures 6A and S6A).

Selinexor, an XPO1 inhibitor, synergistically induces cytotoxicity when combined with MDM2 inhibition in tumor cells.[83,84] We observed expression of XPO1 and MDM2 is high in SHH-3 MB compared to other SHH subtypes (Figures S6B and S6C). We tested idasanutlin either as a single agent or in combination with selinexor to synergistically enhance nuclear p53 activity. *In vitro* cell viability assays demonstrated that idasanutlin potently induced cell death in *ELP1-mutant* MED1712FH and RCMB24 PDX cells (Figure 6B). When combined with selinexor, idasanutlin synergistically promoted tumor cell death in both MED1712FH (IC50: 2.5 nM) and RCMB24 (IC50: 10 nM) PDX (Figures 6B and S6D). In contrast, *ELP1-wildtype* MED113FH PDX cells showed limited sensitivity and drug synergy to idasanutlin and the combination treatment (Figures 6B and S6D).

To assess if p53 mediates idasanutlin-induced cell death, we genetically ablated *TP53* from MED1712FH PDX cells. Loss of p53 abolished idasanutlin-induced cell death and combination treatment synergy compared to parental MED1712FH PDX cells (Figures 6C, S6D and S6E) and partially reduced selinexor-induced cell death, possibly due to p53-independent cytotoxicity of selinexor (Figures S6F and S6G).[86] Western blotting of whole-cell and nuclear p53 levels confirmed idasanutlin treatment, either alone or in combination with selinexor, increased p53 abundance and nuclear p53 activation (p-p53) in *ELP1-mutant* PDX cells, but not in *ELP1-wildtype* PDX cells (Figure 6D). Full-length MDM2 isoform was upregulated in both *ELP1-mutant*, but not *ELP1-wildtype,* PDX cells treated with idasanutlin alone or in combination with selinexor (Figure 6D). These changes in MDM2 isoforms are consistent with p53-MDM2 regulation feedback loops, whereby increased p53 activity upregulates MDM2 to temper p53 levels.[87] These results suggest p53 mediates idasanutlin-induced cell death of *ELP1-mutant* SHH-MB PDX lines.

We genetically validated MDM2 as a therapeutic target in *ELP1-mutant* SHH-MB tumors by knocking out *MDM2* and monitoring its requirement for cell survival using a competition assay. *MDM2* knockout inhibited tumor proliferation compared to a non-targeting control in *ELP1-mutant* MED1712FH PDX cells *in vitro* and *in vivo.* In contrast, *MDM2* knockout did not alter *ELP1-wildtype* MED113FH PDX proliferation (Figures 6E and S6H). Together, our findings indicate that MDM2 inhibition specifically increases nuclear p53 levels to induce cell death in *ELP1-mutant* SHH-MB PDX lines.

We conducted *in vivo* preclinical trials to corroborate *in vitro* findings (Figure S6I). Two rounds of idasanutlin were administered to mice implanted with *ELP1-mutant* MED1712FH and *ELP1-wildtype* MED113FH PDX lines. Idasanutlin alone significantly improved the survival of MED1712FH-bearing mice compared with vehicle-treated controls (median survival time, MST, 52 days vs. 40.5 days), whereas no survival benefit was observed in idasanutlin-treated MED113FH-bearing mice (MST 32 days vs. 31 days) (Figure S6J). We expanded these findings in a second trial using three rounds of idasanutlin treatment either alone or in combination with selinexor. Extended idasanutlin treatment significantly prolonged the survival of MED1712FH-bearing mice compared to vehicle-treated controls (MST 77.5 days vs. 57 days) (Figure 6F). However, the combination of idasanutlin and selinexor failed to improve survival (MST 74 days) compared to idasanutlin treatment alone, although survival improved compared to vehicle-treated controls (MST 57 days) (Figure S6K). Selinexor treatment alone did not improve survival of MED1712FH-bearing mice (MST 60 days). These results suggest the selinexor *in vivo* treatment regimen requires additional optimization. Collectively, these promising preclinical data demonstrate that idasanutlin reactivates p53 signaling and improves survival of *ELP1-mutant* SHH-MB.

DISCUSSION

MBs arising from inherited genetic predisposition to cancer, such as Li-Fraumeni syndrome caused by *TP53* mutations, are characterized by excessive genomic instability and unique mutational signatures.[17,88] In this study, we modeled heterozygous germline *ELP1* LOF, the most prevalent MB genetic predisposition event,[18] to identify mechanisms underlying *ELP1*-mutant SHH-3 MB. We demonstrated that germline *Elp1* deficiency is associated with increased replication stress, DNA damage, aberrant cell cycle, and stalled GNP differentiation, thereby increasing the risk of malignant transformation in the GN lineage. Our studies revealed compromised p53 signaling in *Elp1* LOF

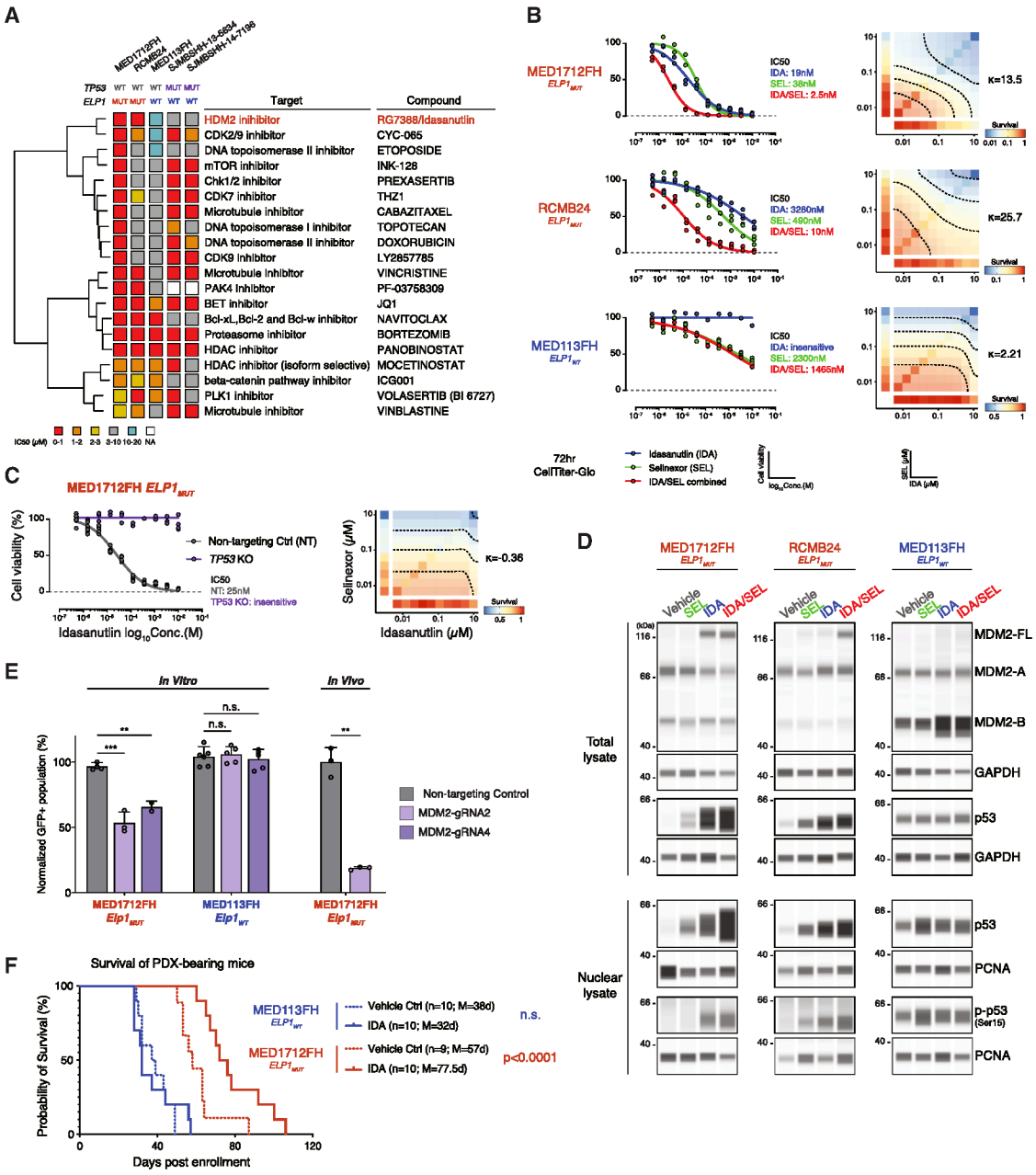

Figure 6. *ELP1*-mutant SHH-MBs are sensitive to MDM2 inhibition

(A) Screen of FDA-approved library of 91 compounds in five SHH-MB PDX tumor lines. Top 20 candidate compounds selected based on the lowest average IC50 values (μM) for *ELP-mutant* lines (MED1712FH and RCMB24).

(B) Representative dose-response curves with IC50 values (left) and BRAID[88] response surface plots with *Kappa* values (right) for idasanutlin (IDA), selinexor (SEL), idasanutlin + selinexor (IDA+SEL) treatments in MED1712FH (*ELP1*-MUT, top), RCMB24 (*ELP1*-MUT, middle), and MED113FH (*ELP1*-WT, bottom) PDX cells. $n \geq 3$ independent experiments.

(C) Representative dose-response curves with IC50 values and BRAID response surface plots with *Kappa* values for IDA treatments in MED1712FH-*TP53KO* and parental MED1712FH PDX cells. $n \geq 3$ independent experiments.

(D) Western blots of MDM2, p53 and GAPDH (loading control) in whole-cell lysates and p53, p-p53 (S15) and PCNA (loading control) in nuclear lysates isolated from Vehicle-, SEL-, IDA-, and IDA+SEL -treated MED1712FH, RCMB24, and MED113FH PDX cells.

(E) Competition assays assessing percentage changes in MED1712FH or MED113FH PDX cells either *in vitro* or *in vivo* after transduction with lentivirus co-expressing GFP and non-targeted control gRNA or *MDM2-KO* (gRNA2 and gRNA4). $n = 2$–5 independent experiments for *in vitro* and $n = 3$ mice for *in vivo* competition assay per group.

(F) Survival curves of MED1712FH and MED113FH PDX-bearing mice receiving Vehicle- or IDA after tumor bioluminescence signals reached threshold ($n \geq 9$ mice per group). Data shown as mean ± SD. (E). Number of mice and median survival for each group indicated in (F). Statistical significance calculated by two-sided *t* test (E) or Log rank Mantel-Cox test (F). $^{**}p < 0.01$, $^{***}p < 0.001$, n.s. $p > 0.05$. See also Figure S6 and Table S6.

GNPs and *Elp1*-deficient SHH-MB tumors and support reactivating p53 activity as a treatment strategy for *ELP1*-associated SHH-MB.

The Elongator complex is essential for efficient transcriptional and translational elongation of long transcripts responsible for neuronal development,[24–32] cell cycle progression,[89–91] and DNA repair machinery.[18,26,63] Translational regulation of cell proliferation versus differentiation in neuronal progenitors is governed by distinct tRNA pools in proliferating versus differentiating cells.[92,93] We confirmed heterozygous germline *ELP1* LOF stalls GNP differentiation, increases actively cycling GNPs and accelerates S-phase, substantiating that the ELP1/Elongator complex is essential for GNP proliferation and differentiation. Hijacked developmental programs and disrupted GNP differentiation is fundamental to the pathogenesis of all SHH-MB subtypes,[41–46] and SHH-3 MB subtype is specifically characterized by actively cycling GNPs.[94] For instance, stalled differentiation increases risk for GNP transformation into SHH-MB in a *Ptch1* heterozygous LOF mouse model.[41] Germline *Elp1* deficiency maintains cycling GNPs in an SHH-responsive state, elevating risk for malignant transformation.

Cerebellar development is characterized by massive postnatal expansion of GNPs, requiring high-fidelity genome duplication.[95] Precise control and coordination of DNA replication with cell cycle checkpoints, DNA repair, and other cellular processes are essential for maintaining genomic stability.[96] Replication stress indicates deregulated DNA replication promoting DNA DSBs, a major source of genomic instability underlying tumorigenesis.[97] We discovered germline *Elp1* deficiency leads to increased replication stress, DNA DSBs, and hyperactive recombination-induced SCE in cycling GNPs. SHH-induced replication stress increases HR and somatic recombination events in GNPs, promoting *Ptch1* loss-of-heterozygosity (LOH) and SHH-MB development in mice.[54] If left unresolved, increased DNA damage and hyperrecombination from germline *ELP1* deficiency could deregulate driver genes capable of initiating GNP transformation.

TP53 and *ELP1* LOF mutations may converge on similar pathways in SHH-3 MB. Our age-stratified culminative risk studies in large patient cohorts identified similar risk for developing SHH-MB (0.3–0.5%) for individuals with germline *ELP1*, *TP53*, or *PTCH1* LOF variants. A subset of *ELP1*-mutant SHH-3 MBs exhibited somatic alterations converging on the p53 pathway, including *PPM1D* (31%) and *MDM4* (10%) amplifications.[18] Our data suggests p53 downregulation via pathogenic *ELP1* germline variation contributes to isochromosome events in SHH-3 MB. At the molecular level, p53/53BP1 maintains replication fork integrity and genomic stability under DNA replication stress[56–61] and senses genomic instability to induce cell cycle arrest, senescence, and apoptosis.[9,14] In GNPs, p53 negatively regulates SHH signaling through *Gli1* and *Gli2*,[14,98–100] and inactivation of p53 signaling permits senescence evasion and progression to malignancy in *Ptch1* LOH-driven SHH-MB mouse models.[15,41] Therefore, inhibition of p53 signaling and accumulating DNA damage could prime GNPs to transformation. Compromised p53/53BP1 signaling observed in both $Elp1_{HET}$ GNPs and $Elp1_{HET}$;$Ptch1_{gRNA}$ tumors provides a plausible mechanistic explanation as to why germline *ELP1* deficiency predisposes GNPs to SHH-3 MB. Mechanisms linking *ELP1* deficiency and compromised p53 signaling warrant future study.

Skeletally mature teenagers and adults with SHH-MB have promising responses to SMO inhibitors in clinical trials; however, limited long-term efficacy supports the development of novel and subtype-specific therapeutics to overcome treatment-induced resistance.[101,102] Understanding the developmental and tumor biology of SHH-MB subtypes, coupled with the engineering of genetically faithful models, can identify therapeutic vulnerabilities as specific and efficient treatment options. Our preclinical evidence leveraging multiple *ELP1*-mutant SHH-MB PDX lines supports idasanutlin, an FDA-approved and BBB-penetrant MDM2 inhibitor,[79,80] as a novel and rational therapy for children affected by *ELP1*-associated SHH-MB.

In summary, we describe a mechanistic and cellular basis for the vulnerability of the GN lineage to *ELP1*-associated SHH-MB development. Importantly, our studies provide complementary *ELP1*-associated SHH-MB mouse models as a resource for future discovery, and immediate clinical direction for the deployment of rational, molecularly informed treatment of children with *ELP1*-associated SHH-MB.

Limitations of the study

Our studies model *ELP1*-associated SHH-MB in the mouse using complementary approaches, faithfully recapitulating histological features and molecular landscapes seen in patient tumors. However, these models had some limitations. $Elp1_{HET}$;$Ptch1_{gRNA}$ tumors did not have biallelic inactivation of *Elp1*, a characteristic of *ELP1*-associated SHH-MB,[18] although we observed ~70–80% reduction in ELP1 protein expression. Since *Elp1* and *Ptch1* map to different chromosomes in the mouse genome, the biallelic inactivation of both *ELP1* and *PTCH1* seen in patient tumors could not be replicated using this model. Moreover, germline *Elp1* deficiency did not increase tumor penetrance or reduce tumor latency in the *Ptch1* model, potentially due to *Ptch1* being a strong tumor driver that overrides the consequences of *Elp1* LOF. Although $Elp1_{gRNA}$;$Ptch1_{gRNA}$;$p53_{null}$ tumors effectively compromised the Elongator complex, genetic inactivation of *TP53* was required for tumorigenesis, which is rare in *ELP1*-mutant SHH-MB patients. Future modeling of *ELP1*-associated SHH-MB in human cerebellar organoids could overcome species-related limitations.

RESOURCE AVAILABILITY

Lead contact

Further information and requests for resources and reagents should be directed to and will be fulfilled by the lead contact, Dr. Paul. A. Northcott (paul.northcott@stjude.org).

Materials availability

All materials generated in this study are available from the lead contact upon request with appropriate materials transfer agreement.

Data and code availability

The scRNA-seq, bulk RNA-seq, WGS, and DNA methylation data supporting the findings of this study have been deposited in BioProject: PRJNA1083708. Expression data are available in GEO: GSE260851. Proteomic datasets from mouse tumor and GNPs have been deposited in PRIDE: PXD050487 and PXD050488. Any additional information required to analyze the data in this paper is available from the lead contact upon request.

ACKNOWLEDGMENTS

This work was principally supported by the American Lebanese Syrian Associated Charities and St. Jude (P.A.N.), St. Baldrick's Foundation (Robert J. Arceci Innovation Award; P.A.N.), and the National Cancer Institute (P.A.N., M.F.R., and S.J.B., P01CA096832; P.A.N., 1R01CA270785), and the Cancer Center Support Grant (P.A.N., M.F.R., and S.J.B., P30CA021765). L.M.K. was supported by a DFG Individual Grant (#497317859). From St. Jude, we explicitly acknowledge the following shared resources: Center for Advanced Genome Engineering, Cell and Tissue Imaging Center, Hartwell Center for Biotechnology, Center for In Vivo Imaging and Therapeutics, Cytogenetics, and Preclinical Therapeutics Program, Comparative Pathological Core, Center for Proteomics and Metabolomics, Animal Resource Center, and Analytical Technologies Center-Preclinical Formulation. We thank Kim Lowe in DNB Flow Cytometry Core for FACS assistance.

AUTHOR CONTRIBUTIONS

P.A.N. supervised the study and provided funding. S.T.A., J.G.-L, Y.L., H.L., and P.A.N. designed the study. S.T.A., J.G.-L, Y.L., H.L., B.G., and S.M.W. performed experiments and analyzed data; J.H., L.P., A.A., M.B., T.S., F.M., F.Z., M.K., A.M., B.B., and M.L. performed experiments. A.P. and A.S. performed image quantification analysis. N.R.T. performed drug synergy analysis. S.C.W. contributed to graphic design and enhanced the imaging quality of manuscript figures for the paper revision. S.A.L. assisted in editing and refining the manuscript text for the paper revision. L.J. and B.A.O. performed histological evaluation; S.J.B., M.F.R., Z.R., A.G., G.W.R., C.T., S.M.W., B.W., A.A.S., S.M.P., and L.M.K. advised on the experimental design. S.T.A., J.G.-L., Y.L., H.L., and P.A.N. wrote the manuscript. All authors read and approved the final version of the manuscript.

DECLARATION OF INTERESTS

All authors declare no conflict of interests.

STAR★METHODS

Detailed methods are provided in the online version of this paper and include the following:

SUPPLEMENTAL INFORMATION

Supplemental information can be found online at https://doi.org/10.1016/j.ccell.2025.04.014.

Received: March 10, 2024
Revised: February 23, 2025
Accepted: April 28, 2025
Published: May 15, 2025

REFERENCES

1. Northcott, P.A., Robinson, G.W., Kratz, C.P., Mabbott, D.J., Pomeroy, S.L., Clifford, S.C., Rutkowski, S., Ellison, D.W., Malkin, D., Taylor, M.D., et al. (2019). Medulloblastoma. Nat. Rev. Dis. Primers *5*, 11. https://doi.org/10.1038/s41572-019-0063-6.
2. Garcia-Lopez, J., Kumar, R., Smith, K.S., and Northcott, P.A. (2021). Deconstructing Sonic Hedgehog Medulloblastoma: Molecular Subtypes, Drivers, and Beyond. Trends Genet. *37*, 235–250. https://doi.org/10.1016/j.tig.2020.11.001.
3. Goodrich, L.V., Milenković, L., Higgins, K.M., and Scott, M.P. (1997). Altered neural cell fates and medulloblastoma in mouse patched mutants. Science *277*, 1109–1113. https://doi.org/10.1126/science.277.5329.1109.
4. Yang, Z.J., Ellis, T., Markant, S.L., Read, T.A., Kessler, J.D., Bourboulas, M., Schüller, U., Machold, R., Fishell, G., Rowitch, D.H., et al. (2008). Medulloblastoma can be initiated by deletion of Patched in lineage-restricted progenitors or stem cells. Cancer Cell *14*, 135–145. https://doi.org/10.1016/j.ccr.2008.07.003.
5. Schuller, U., Heine, V.M., Mao, J., Kho, A.T., Dillon, A.K., Han, Y.G., Huillard, E., Sun, T., Ligon, A.H., Qian, Y., et al. (2008). Acquisition of granule neuron precursor identity is a critical determinant of progenitor cell competence to form Shh-induced medulloblastoma. Cancer Cell *14*, 123–134. https://doi.org/10.1016/j.ccr.2008.07.005.
6. Oliver, T.G., Read, T.A., Kessler, J.D., Mehmeti, A., Wells, J.F., Huynh, T.T.T., Lin, S.M., and Wechsler-Reya, R.J. (2005). Loss of patched and disruption of granule cell development in a pre-neoplastic stage of medulloblastoma. Development *132*, 2425–2439. https://doi.org/10.1242/dev.01793.
7. Hatten, M.E., and Heintz, N. (1995). Mechanisms of neural patterning and specification in the developing cerebellum. Annu. Rev. Neurosci. *18*, 385–408. https://doi.org/10.1146/annurev.ne.18.030195.002125.
8. Wechsler-Reya, R.J., and Scott, M.P. (1999). Control of neuronal precursor proliferation in the cerebellum by Sonic Hedgehog. Neuron *22*, 103–114. https://doi.org/10.1016/s0896-6273(00)80682-0.
9. McKinnon, P.J. (2017). Genome integrity and disease prevention in the nervous system. Genes Dev. *31*, 1180–1194. https://doi.org/10.1101/gad.301325.117.

10. Williams, J.S., Lujan, S.A., and Kunkel, T.A. (2016). Processing ribonucleotides incorporated during eukaryotic DNA replication. Nat. Rev. Mol. Cell Biol. *17*, 350–363. https://doi.org/10.1038/nrm.2016.37.

11. McKinnon, P.J. (2016). Topoisomerases and the regulation of neural function. Nat. Rev. Neurosci. *17*, 673–679. https://doi.org/10.1038/nrn.2016.101.

12. Hamperl, S., and Cimprich, K.A. (2016). Conflict Resolution in the Genome: How Transcription and Replication Make It Work. Cell *167*, 1455–1467. https://doi.org/10.1016/j.cell.2016.09.053.

13. Berti, M., and Vindigni, A. (2016). Replication stress: getting back on track. Nat. Struct. Mol. Biol. *23*, 103–109. https://doi.org/10.1038/nsmb.3163.

14. Barthelery, N.J., and Manfredi, J.J. (2016). Cerebellum Development and Tumorigenesis: A p53-Centric Perspective. Trends Mol. Med. *22*, 404–413. https://doi.org/10.1016/j.molmed.2016.03.006.

15. Tamayo-Orrego, L., Swikert, S.M., and Charron, F. (2016). Evasion of cell senescence in SHH medulloblastoma. Cell Cycle *15*, 2102–2107. https://doi.org/10.1080/15384101.2016.1189044.

16. Ramaswamy, V., Nör, C., and Taylor, M.D. (2015). p53 and Meduloblastoma. Cold Spring Harb. Perspect. Med. *6*, a026278. https://doi.org/10.1101/cshperspect.a026278.

17. Waszak, S.M., Northcott, P.A., Buchhalter, I., Robinson, G.W., Sutter, C., Groebner, S., Grund, K.B., Brugières, L., Jones, D.T.W., Pajtler, K.W., et al. (2018). Spectrum and prevalence of genetic predisposition in medulloblastoma: a retrospective genetic study and prospective validation in a clinical trial cohort. Lancet Oncol. *19*, 785–798. https://doi.org/10.1016/S1470-2045(18)30242-0.

18. Waszak, S.M., Robinson, G.W., Gudenas, B.L., Smith, K.S., Forget, A., Kojic, M., Garcia-Lopez, J., Hadley, J., Hamilton, K.V., Indersie, E., et al. (2020). Germline Elongator mutations in Sonic Hedgehog medulloblastoma. Nature *580*, 396–401. https://doi.org/10.1038/s41586-020-2164-5.

19. Jovanovic, A., Tosic, N., Marjanovic, I., Komazec, J., Zukic, B., Nikitovic, M., Ilic, R., Grujicic, D., Janic, D., and Pavlovic, S. (2023). Germline Variants in Cancer Predisposition Genes in Pediatric Patients with Central Nervous System Tumors. Int. J. Mol. Sci. *24*, 17387. https://doi.org/10.3390/ijms242417387.

20. Guerrini-Rousseau, L., Masliah-Planchon, J., Filser, M., Tauziède-Espariat, A., Entz-Werle, N., Maugard, C.M., Hopman, S.M.J., Torrejon, J., Gauthier-Villars, M., Simaga, F., et al. (2024). Medulloblastomas with ELP1 pathogenic variants: A weakly penetrant syndrome with a restricted spectrum in a limited age window. Neurooncol. Adv. *6*, vdae075. https://doi.org/10.1093/noajnl/vdae075.

21. Smith, M.J., Woodward, E.R., and Evans, D.G. (2023). Perspectives on the implications of carrying putative pathogenic variants in the medulloblastoma predisposition genes ELP1 and GPR161. Fam. Cancer *22*, 341–344. https://doi.org/10.1007/s10689-023-00330-7.

22. Johansson, M.J.O., Xu, F., and Byström, A.S. (2018). Elongator-a tRNA modifying complex that promotes efficient translational decoding. Biochim. Biophys. Acta. Gene Regul. Mech. *1861*, 401–408. https://doi.org/10.1016/j.bbagrm.2017.11.006.

23. Karlsborn, T., Tükenmez, H., Mahmud, A.K.M.F., Xu, F., Xu, H., and Byström, A.S. (2014). Elongator, a conserved complex required for wobble uridine modifications in eukaryotes. RNA Biol. *11*, 1519–1528. https://doi.org/10.4161/15476286.2014.992276.

24. Chaverra, M., George, L., Mergy, M., Waller, H., Kujawa, K., Murnion, C., Sharples, E., Thorne, J., Podgajny, N., Grindeland, A., et al. (2017). The familial dysautonomia disease gene IKBKAP is required in the developing and adult mouse central nervous system. Dis. Model. Mech. *10*, 605–618. https://doi.org/10.1242/dmm.028258.

25. George, L., Chaverra, M., Wolfe, L., Thorne, J., Close-Davis, M., Eibs, A., Riojas, V., Grindeland, A., Orr, M., Carlson, G.A., and Lefcort, F. (2013). Familial dysautonomia model reveals Ikbkap deletion causes apoptosis of Pax3+ progenitors and peripheral neurons. Proc. Natl. Acad. Sci. USA *110*, 18698–18703. https://doi.org/10.1073/pnas.1308596110.

26. Goffena, J., Lefcort, F., Zhang, Y., Lehrmann, E., Chaverra, M., Felig, J., Walters, J., Buksch, R., Becker, K.G., and George, L. (2018). Elongator and codon bias regulate protein levels in mammalian peripheral neurons. Nat. Commun. *9*, 889. https://doi.org/10.1038/s41467-018-03221-z.

27. Hunnicutt, B.J., Chaverra, M., George, L., and Lefcort, F. (2012). IKAP/Elp1 is required in vivo for neurogenesis and neuronal survival, but not for neural crest migration. PLoS One *7*, e32050. https://doi.org/10.1371/journal.pone.0032050.

28. Tolman, Z., Chaverra, M., George, L., and Lefcort, F. (2022). Elp1 is required for development of visceral sensory peripheral and central circuitry. Dis. Model. Mech. *15*, dmm049274. https://doi.org/10.1242/dmm.049274.

29. Arnskotter, F., da Silva, P.B.G., Schouw, M.E., Lukasch, C., Bianchini, L., Sieber, L., Garcia-Lopez, J., Ahmad, S.T., Li, Y., Lin, H., et al. (2024). Loss of Elp1 in cerebellar granule cell progenitors models ataxia phenotype of Familial Dysautonomia. Neurobiol. Dis. *199*, 106600. https://doi.org/10.1016/j.nbd.2024.106600.

30. Morini, E., Gao, D., Logan, E.M., Salani, M., Krauson, A.J., Chekuri, A., Chen, Y.T., Ragavendran, A., Chakravarty, P., Erdin, S., et al. (2022). Developmental regulation of neuronal gene expression by Elongator complex protein 1 dosage. J Genet Genomics *49*, 654–665. https://doi.org/10.1016/j.jgg.2021.11.011.

31. Morini, E., Gao, D., Montgomery, C.M., Salani, M., Mazzasette, C., Krussig, T.A., Swain, B., Dietrich, P., Narasimhan, J., Gabbeta, V., et al. (2019). ELP1 Splicing Correction Reverses Proprioceptive Sensory Loss in Familial Dysautonomia. Am. J. Hum. Genet. *104*, 638–650. https://doi.org/10.1016/j.ajhg.2019.02.009.

32. Gaik, M., Kojic, M., Wainwright, B.J., and Glatt, S. (2023). Elongator and the role of its subcomplexes in human diseases. EMBO Mol. Med. *15*, e16418. https://doi.org/10.15252/emmm.202216418.

33. Ostrom, Q.T., Price, M., Neff, C., Cioffi, G., Waite, K.A., Kruchko, C., and Barnholtz-Sloan, J.S. (2023). CBTRUS Statistical Report: Primary Brain and Other Central Nervous System Tumors Diagnosed in the United States in 2016-2020. Neuro Oncol. *25*, iv1–iv99. https://doi.org/10.1093/neuonc/noad149.

34. Song, H., Dicks, E., Ramus, S.J., Tyrer, J.P., Intermaggio, M.P., Hayward, J., Edlund, C.K., Conti, D., Harrington, P., Fraser, L., et al. (2015). Contribution of Germline Mutations in the RAD51B, RAD51C, and RAD51D Genes to Ovarian Cancer in the Population. J. Clin. Oncol. *33*, 2901–2907. https://doi.org/10.1200/JCO.2015.61.2408.

35. Karczewski, K.J., Solomonson, M., Chao, K.R., Goodrich, J.K., Tiao, G., Lu, W., Riley-Gillis, B.M., Tsai, E.A., Kim, H.I., Zheng, X., et al. (2022). Systematic single-variant and gene-based association testing of thousands of phenotypes in 394,841 UK Biobank exomes. Cell Genom. *2*, 100168. https://doi.org/10.1016/j.xgen.2022.100168.

36. de Andrade, K.C., Frone, M.N., Wegman-Ostrosky, T., Khincha, P.P., Kim, J., Amadou, A., Santiago, K.M., Fortes, F.P., Lemonnier, N., Mirabello, L., et al. (2019). Variable population prevalence estimates of germline TP53 variants: A gnomAD-based analysis. Hum. Mutat. *40*, 97–105. https://doi.org/10.1002/humu.23673.

37. Guerrini-Rousseau, L., Smith, M.J., Kratz, C.P., Doergeloh, B., Hirsch, S., Hopman, S.M.J., Jorgensen, M., Kuhlen, M., Michaeli, O., Milde, T., et al. (2021). Current recommendations for cancer surveillance in Gorlin syndrome: a report from the SIOPE host genome working group (SIOPE HGWG). Fam. Cancer *20*, 317–325. https://doi.org/10.1007/s10689-021-00247-z.

38. Harms, D.W., Quadros, R.M., Seruggia, D., Ohtsuka, M., Takahashi, G., Montoliu, L., and Gurumurthy, C.B. (2014). Mouse Genome Editing Using the CRISPR/Cas System. Curr. Protoc. Hum. Genet. *83*, 15.7.1–15.7.27. https://doi.org/10.1002/0471142905.hg1507s83.

39. Chen, Y.T., Hims, M.M., Shetty, R.S., Mull, J., Liu, L., Leyne, M., and Slaugenhaupt, S.A. (2009). Loss of mouse Ikbkap, a subunit of elongator, leads to transcriptional deficits and embryonic lethality that can be rescued by human IKBKAP. Mol. Cell Biol. *29*, 736–744. https://doi.org/10.1128/MCB.01313-08.

40. Xu, H., Lin, Z., Li, F., Diao, W., Dong, C., Zhou, H., Xie, X., Wang, Z., Shen, Y., and Long, J. (2015). Dimerization of elongator protein 1 is essential for Elongator complex assembly. Proc. Natl. Acad. Sci. USA *112*, 10697–10702. https://doi.org/10.1073/pnas.1502597112.

41. Ayrault, O., Zhao, H., Zindy, F., Qu, C., Sherr, C.J., and Roussel, M.F. (2010). Atoh1 inhibits neuronal differentiation and collaborates with Gli1 to generate medulloblastoma-initiating cells. Cancer Res. *70*, 5618–5627. https://doi.org/10.1158/0008-5472.CAN-09-3740.

42. Hovestadt, V., Smith, K.S., Bihannic, L., Filbin, M.G., Shaw, M.L., Baumgartner, A., DeWitt, J.C., Groves, A., Mayr, L., Weisman, H.R., et al. (2019). Resolving medulloblastoma cellular architecture by single-cell genomics. Nature *572*, 74–79. https://doi.org/10.1038/s41586-019-1434-6.

43. Tao, R., Han, K., Wu, S.C., Friske, J.D., Roussel, M.F., and Northcott, P. A. (2025). Arrested development: the dysfunctional life history of medulloblastoma. Genes Dev. *39*, 4–17. https://doi.org/10.1101/gad.351936.124.

44. Luo, W., Lin, G.N., Song, W., Zhang, Y., Lai, H., Zhang, M., Miao, J., Cheng, X., Wang, Y., Li, W., et al. (2021). Single-cell spatial transcriptomic analysis reveals common and divergent features of developing postnatal granule cerebellar cells and medulloblastoma. BMC Biol. *19*, 135. https://doi.org/10.1186/s12915-021-01071-8.

45. Yang, R., Wang, M., Wang, J., Huang, X., Yang, R., and Gao, W.Q. (2015). Cell Division Mode Change Mediates the Regulation of Cerebellar Granule Neurogenesis Controlled by the Sonic Hedgehog Signaling. Stem Cell Rep. *5*, 816–828. https://doi.org/10.1016/j.stemcr.2015.09.019.

46. Jessa, S., Blanchet-Cohen, A., Krug, B., Vladoiu, M., Coutelier, M., Faury, D., Poreau, B., De Jay, N., Hébert, S., Monlong, J., et al. (2019). Stalled developmental programs at the root of pediatric brain tumors. Nat. Genet. *51*, 1702–1713. https://doi.org/10.1038/s41588-019-0531-7.

47. Rose, M.F., Ren, J., Ahmad, K.A., Chao, H.T., Klisch, T.J., Flora, A., Greer, J.J., and Zoghbi, H.Y. (2009). Math1 is essential for the development of hindbrain neurons critical for perinatal breathing. Neuron *64*, 341–354. https://doi.org/10.1016/j.neuron.2009.10.023.

48. Fagundes, R., and Teixeira, L.K. (2021). Cyclin E/CDK2: DNA Replication, Replication Stress and Genomic Instability. Front. Cell Dev. Biol. *9*, 774845. https://doi.org/10.3389/fcell.2021.774845.

49. Hughes, B.T., Sidorova, J., Swanger, J., Monnat, R.J., Jr., and Clurman, B.E. (2013). Essential role for Cdk2 inhibitory phosphorylation during replication stress revealed by a human Cdk2 knockin mutation. Proc. Natl. Acad. Sci. USA *110*, 8954–8959. https://doi.org/10.1073/pnas.1302927110.

50. Saxena, S., and Zou, L. (2022). Hallmarks of DNA replication stress. Mol. Cell *82*, 2298–2314. https://doi.org/10.1016/j.molcel.2022.05.004.

51. Toledo, L.I., Altmeyer, M., Rask, M.B., Lukas, C., Larsen, D.H., Povlsen, L.K., Bekker-Jensen, S., Mailand, N., Bartek, J., and Lukas, J. (2013). ATR prohibits replication catastrophe by preventing global exhaustion of RPA. Cell *155*, 1088–1103. https://doi.org/10.1016/j.cell.2013.10.043.

52. Techer, H., Koundrioukoff, S., Nicolas, A., and Debatisse, M. (2017). The impact of replication stress on replication dynamics and DNA damage in vertebrate cells. Nat. Rev. Genet. *18*, 535–550. https://doi.org/10.1038/nrg.2017.46.

53. Crozier, L., Foy, R., Mouery, B.L., Whitaker, R.H., Corno, A., Spanos, C., Ly, T., Gowen Cook, J., and Saurin, A.T. (2022). CDK4/6 inhibitors induce replication stress to cause long-term cell cycle withdrawal. EMBO J. *41*, e108599. https://doi.org/10.15252/embj.2021108599.

54. Tamayo-Orrego, L., Gallo, D., Racicot, F., Bemmo, A., Mohan, S., Ho, B., Salameh, S., Hoang, T., Jackson, A.P., Brown, G.W., and Charron, F. (2020). Sonic hedgehog accelerates DNA replication to cause replication stress promoting cancer initiation in medulloblastoma. Nat. Cancer *1*, 840–854. https://doi.org/10.1038/s43018-020-0094-7.

55. Cuella-Martin, R., Oliveira, C., Lockstone, H.E., Snellenberg, S., Grolmusova, N., and Chapman, J.R. (2016). 53BP1 Integrates DNA Repair and p53-Dependent Cell Fate Decisions via Distinct Mechanisms. Mol. Cell *64*, 51–64. https://doi.org/10.1016/j.molcel.2016.08.002.

56. Her, J., Ray, C., Altshuler, J., Zheng, H., and Bunting, S.F. (2018). 53BP1 Mediates ATR-Chk1 Signaling and Protects Replication Forks under Conditions of Replication Stress. Mol. Cell Biol. *38*, e00472-17. https://doi.org/10.1128/MCB.00472-17.

57. Tripathi, V., Kaur, S., and Sengupta, S. (2008). Phosphorylation-dependent interactions of BLM and 53BP1 are required for their anti-recombinogenic roles during homologous recombination. Carcinogenesis *29*, 52–61. https://doi.org/10.1093/carcin/bgm238.

58. Tripathi, V., Nagarjuna, T., and Sengupta, S. (2007). BLM helicase-dependent and -independent roles of 53BP1 during replication stress-mediated homologous recombination. J. Cell Biol. *178*, 9–14. https://doi.org/10.1083/jcb.200610051.

59. Sengupta, S., Linke, S.P., Pedeux, R., Yang, Q., Farnsworth, J., Garfield, S.H., Valerie, K., Shay, J.W., Ellis, N.A., Wasylyk, B., and Harris, C.C. (2003). BLM helicase-dependent transport of p53 to sites of stalled DNA replication forks modulates homologous recombination. EMBO J. *22*, 1210–1222. https://doi.org/10.1093/emboj/cdg114.

60. Zhang, L., Geng, X., Wang, F., Tang, J., Ichida, Y., Sharma, A., Jin, S., Chen, M., Tang, M., Pozo, F.M., et al. (2022). 53BP1 regulates heterochromatin through liquid phase separation. Nat. Commun. *13*, 360. https://doi.org/10.1038/s41467-022-28019-y.

61. Soussi, T., and Kroemer, G. (2017). TP53 and 53BP1 Reunited. Trends Cell Biol. *27*, 311–313. https://doi.org/10.1016/j.tcb.2016.10.004.

62. Ait Saada, A., Lambert, S.A.E., and Carr, A.M. (2018). Preserving replication fork integrity and competence via the homologous recombination pathway. DNA Repair *71*, 135–147. https://doi.org/10.1016/j.dnarep.2018.08.017.

63. Chen, W.T., Tseng, H.Y., Jiang, C.L., Lee, C.Y., Chi, P., Chen, L.Y., Lo, K. Y., Wang, I.C., and Lin, F.J. (2021). Elp1 facilitates RAD51-mediated homologous recombination repair via translational regulation. J. Biomed. Sci. *28*, 81. https://doi.org/10.1186/s12929-021-00773-z.

64. Panier, S., and Boulton, S.J. (2014). Double-strand break repair: 53BP1 comes into focus. Nat. Rev. Mol. Cell Biol. *15*, 7–18. https://doi.org/10.1038/nrm3719.

65. Stults, D.M., Killen, M.W., and Pierce, A.J. (2014). The sister chromatid exchange (SCE) assay. Methods Mol. Biol. *1105*, 439–455. https://doi.org/10.1007/978-1-62703-739-6_32.

66. Tuna, M., Amos, C.I., and Mills, G.B. (2022). Whole-chromosome arm acquired uniparental disomy in cancer development is a consequence of isochromosome formation. Neoplasia *25*, 9–17. https://doi.org/10.1016/j.neo.2021.12.009.

67. Capper, D., Jones, D.T.W., Sill, M., Hovestadt, V., Schrimpf, D., Sturm, D., Koelsche, C., Sahm, F., Chavez, L., Reuss, D.E., et al. (2018). DNA methylation-based classification of central nervous system tumours. Nature *555*, 469–474. https://doi.org/10.1038/nature26000.

68. Ellison, D.W., Dalton, J., Kocak, M., Nicholson, S.L., Fraga, C., Neale, G., Kenney, A.M., Brat, D.J., Perry, A., Yong, W.H., et al. (2011). Medulloblastoma: clinicopathological correlates of SHH, WNT, and non-SHH/WNT molecular subgroups. Acta Neuropathol. *121*, 381–396. https://doi.org/10.1007/s00401-011-0800-8.

69. Fernandez-L, A., Northcott, P.A., Dalton, J., Fraga, C., Ellison, D., Angers, S., Taylor, M.D., and Kenney, A.M. (2009). YAP1 is amplified and up-regulated in hedgehog-associated medulloblastomas and mediates Sonic hedgehog-driven neural precursor proliferation. Genes Dev. *23*, 2729–2741. https://doi.org/10.1101/gad.1824509.

70. Finkel, T., and Hwang, P.M. (2009). The Krebs cycle meets the cell cycle: mitochondria and the G1-S transition. Proc. Natl. Acad. Sci. USA *106*, 11825–11826. https://doi.org/10.1073/pnas.0906430106.

71. Koval, O.M., Nguyen, E.K., Santhana, V., Fidler, T.P., Sebag, S.C., Rasmussen, T.P., Mittauer, D.J., Strack, S., Goswami, P.C., Abel, E.D., and Grumbach, I.M. (2019). Loss of MCU prevents mitochondrial fusion

in G(1)-S phase and blocks cell cycle progression and proliferation. Sci. Signal. *12*, eaav1439. https://doi.org/10.1126/scisignal.aav1439.

72. Mochizuki-Kashio, M., Otsuki, N., Fujiki, K., Abdelhamd, S., Kurre, P., Grompe, M., Iwama, A., Saito, K., and Nakamura-Ishizu, A. (2023). Replication stress increases mitochondrial metabolism and mitophagy in FANCD2 deficient fetal liver hematopoietic stem cells. Front. Oncol. *13*, 1108430. https://doi.org/10.3389/fonc.2023.1108430.
73. Ozaki, T., and Nakagawara, A. (2011). Role of p53 in Cell Death and Human Cancers. Cancers *3*, 994–1013. https://doi.org/10.3390/cancers3010994.
74. Frazier, D.P., Kendig, R.D., Kai, F., Maglic, D., Sugiyama, T., Morgan, R. L., Fry, E.A., Lagedrost, S.J., Sui, G., and Inoue, K. (2012). Dmp1 physically interacts with p53 and positively regulates p53's stability, nuclear localization, and function. Cancer Res. *72*, 1740–1750. https://doi.org/10.1158/0008-5472.CAN-11-2410.
75. Inoue, T., Wu, L., Stuart, J., and Maki, C.G. (2005). Control of p53 nuclear accumulation in stressed cells. FEBS Lett. *579*, 4978–4984. https://doi.org/10.1016/j.febslet.2005.08.006.
76. Ohlen, S.B., Russell, M.L., Brownstein, M.J., and Lefcort, F. (2017). BGP-15 prevents the death of neurons in a mouse model of familial dysautonomia. Proc. Natl. Acad. Sci. USA *114*, 5035–5040. https://doi.org/10.1073/pnas.1620212114.
77. Jonchere, B., Williams, J., Zindy, F., Liu, J., Robinson, S., Farmer, D.M., Min, J., Yang, L., Stripay, J.L., Wang, Y., et al. (2023). Combination of Ribociclib with BET-Bromodomain and PI3K/mTOR Inhibitors for Medulloblastoma Treatment In Vitro and In Vivo. Mol. Cancer Ther. *22*, 37–51. https://doi.org/10.1158/1535-7163.MCT-21-0896.
78. Smith, K.S., Xu, K., Mercer, K.S., Boop, F., Klimo, P., DeCupyere, M., Grenet, J., Robinson, S., Dunphy, P., Baker, S.J., et al. (2020). Patient-derived orthotopic xenografts of pediatric brain tumors: a St. Jude resource. Acta Neuropathol. *140*, 209–225. https://doi.org/10.1007/s00401-020-02171-5.
79. Xu, C., Liu, H., Pirozzi, C.J., Chen, L.H., Greer, P.K., Diplas, B.H., Zhang, L., Waitkus, M.S., He, Y., and Yan, H. (2021). TP53 wild-type/PPM1D mutant diffuse intrinsic pontine gliomas are sensitive to a MDM2 antagonist. Acta Neuropathol. Commun. *9*, 178. https://doi.org/10.1186/s40478-021-01270-y.
80. Ding, Q., Zhang, Z., Liu, J.J., Jiang, N., Zhang, J., Ross, T.M., Chu, X.J., Bartkovitz, D., Podlaski, F., Janson, C., et al. (2013). Discovery of RG7388, a potent and selective p53-MDM2 inhibitor in clinical development. J. Med. Chem. *56*, 5979–5983. https://doi.org/10.1021/jm400487c.
81. Rudolph, J., Crawford, J.J., Hoeflich, K.P., and Wang, W. (2015). Inhibitors of p21-activated kinases (PAKs). J. Med. Chem. *58*, 111–129. https://doi.org/10.1021/jm501613q.
82. Li, Y., Lu, Q., Xie, C., Yu, Y., and Zhang, A. (2022). Recent advances on development of p21-activated kinase 4 inhibitors as anti-tumor agents. Front. Pharmacol. *13*, 956220. https://doi.org/10.3389/fphar.2022.956220.
83. Nishida, Y., Ishizawa, J., Ayoub, E., Montoya, R.H., Ostermann, L.B., Muftuoglu, M., Ruvolo, V.R., Patsilevas, T., Scruggs, D.A., Khazaei, S., et al. (2023). Enhanced TP53 reactivation disrupts MYC transcriptional program and overcomes venetoclax resistance in acute myeloid leukemias. Sci. Adv. *9*, eadh1436. https://doi.org/10.1126/sciadv.adh1436.
84. Alzahrani, A., Natarajan, U., and Rathinavelu, A. (2022). Enhancement of MDM2 inhibitory effects through blocking nuclear export mechanisms in ovarian cancer cells. Cancer Genet. *266–267*, 57–68. https://doi.org/10.1016/j.cancergen.2022.06.003.
85. Twarog, N.R., Stewart, E., Hammill, C.V., and Shelat, A.A. (2016). BRAID: A Unifying Paradigm for the Analysis of Combined Drug Action. Sci. Rep. *6*, 25523. https://doi.org/10.1038/srep25523.
86. Wahba, A., Rath, B.H., O'Neill, J.W., Camphausen, K., and Tofilon, P.J. (2018). The XPO1 Inhibitor Selinexor Inhibits Translation and Enhances the Radiosensitivity of Glioblastoma Cells Grown In Vitro and In Vivo. Mol. Cancer Ther. *17*, 1717–1726. https://doi.org/10.1158/1535-7163.MCT-17-1303.
87. Zheng, T., Wang, J., Zhao, Y., Zhang, C., Lin, M., Wang, X., Yu, H., Liu, L., Feng, Z., and Hu, W. (2013). Spliced MDM2 isoforms promote mutant p53 accumulation and gain-of-function in tumorigenesis. Nat. Commun. *4*, 2996. https://doi.org/10.1038/ncomms3996.
88. Carta, R., Del Baldo, G., Miele, E., Po, A., Besharat, Z.M., Nazio, F., Colafati, G.S., Piccirilli, E., Agolini, E., Rinelli, M., et al. (2020). Cancer Predisposition Syndromes and Medulloblastoma in the Molecular Era. Front. Oncol. *10*, 566822. https://doi.org/10.3389/fonc.2020.566822.
89. Bauer, F., Matsuyama, A., Candiracci, J., Dieu, M., Scheliga, J., Wolf, D. A., Yoshida, M., and Hermand, D. (2012). Translational control of cell division by Elongator. Cell Rep. *1*, 424–433. https://doi.org/10.1016/j.celrep.2012.04.001.
90. Gu, J., Sun, D., Zheng, Q., Wang, X., Yang, H., Miao, J., Jiang, J., and Wei, W. (2009). Human Elongator complex is involved in cell cycle and suppresses cell growth in 293T human embryonic kidney cells. Acta Biochim. Biophys. Sin. *41*, 831–838. https://doi.org/10.1093/abbs/gmp072.
91. Planelles-Herrero, V.J., Bittleston, A., Seum, C., Daeden, A., Gaitan, M. G., and Derivery, E. (2022). Elongator stabilizes microtubules to control central spindle asymmetry and polarized trafficking of cell fate determinants. Nat. Cell Biol. *24*, 1606–1616. https://doi.org/10.1038/s41556-022-01020-9.
92. Gingold, H., Tehler, D., Christoffersen, N.R., Nielsen, M.M., Asmar, F., Kooistra, S.M., Christophersen, N.S., Christensen, L.L., Borre, M., Sørensen, K.D., et al. (2014). A dual program for translation regulation in cellular proliferation and differentiation. Cell *158*, 1281–1292. https://doi.org/10.1016/j.cell.2014.08.011.
93. Guimaraes, J.C., Mittal, N., Gnann, A., Jedlinski, D., Riba, A., Buczak, K., Schmidt, A., and Zavolan, M. (2020). A rare codon-based translational program of cell proliferation. Genome Biol. *21*, 44. https://doi.org/10.1186/s13059-020-1943-5.
94. Gold, M.P., Ong, W., Masteller, A.M., Ghasemi, D.R., Galindo, J.A., Park, N.R., Huynh, N.C., Donde, A., Pister, V., Saurez, R.A., et al. (2024). Developmental basis of SHH medulloblastoma heterogeneity. Nat. Commun. *15*, 270. https://doi.org/10.1038/s41467-023-44300-0.
95. Butts, T., Chaplin, N., and Wingate, R.J.T. (2011). Can clues from evolution unlock the molecular development of the cerebellum? Mol. Neurobiol. *43*, 67–76. https://doi.org/10.1007/s12035-010-8160-2.
96. Feng, J., Liang, J., Li, J., Li, Y., Liang, H., Zhao, X., McNutt, M.A., and Yin, Y. (2015). PTEN Controls the DNA Replication Process through MCM2 in Response to Replicative Stress. Cell Rep. *13*, 1295–1303. https://doi.org/10.1016/j.celrep.2015.10.016.
97. Negrini, S., Gorgoulis, V.G., and Halazonetis, T.D. (2010). Genomic instability–an evolving hallmark of cancer. Nat. Rev. Mol. Cell Biol. *11*, 220–228. https://doi.org/10.1038/nrm2858.
98. Malek, R., Matta, J., Taylor, N., Perry, M.E., and Mendrysa, S.M. (2011). The p53 inhibitor MDM2 facilitates Sonic Hedgehog-mediated tumorigenesis and influences cerebellar foliation. PLoS One *6*, e17884. https://doi.org/10.1371/journal.pone.0017884.
99. Po, A., Ferretti, E., Miele, E., De Smaele, E., Paganelli, A., Canettieri, G., Coni, S., Di Marcotullio, L., Biffoni, M., Massimi, L., et al. (2010). Hedgehog controls neural stem cells through p53-independent regulation of Nanog. EMBO J. *29*, 2646–2658. https://doi.org/10.1038/emboj.2010.131.
100. Stecca, B., and Ruiz i Altaba, A. (2009). A GLI1-p53 inhibitory loop controls neural stem cell and tumour cell numbers. EMBO J. *28*, 663–676. https://doi.org/10.1038/emboj.2009.16.
101. Li, Q.R., Zhao, H., Zhang, X.S., Lang, H., and Yu, K. (2019). Novel-smoothened inhibitors for therapeutic targeting of naive and drug-resistant hedgehog pathway-driven cancers. Acta Pharmacol. Sin. *40*, 257–267. https://doi.org/10.1038/s41401-018-0019-5.
102. Yauch, R.L., Dijkgraaf, G.J.P., Alicke, B., Januario, T., Ahn, C.P., Holcomb, T., Pujara, K., Stinson, J., Callahan, C.A., Tang, T., et al. (2009). Smoothened mutation confers resistance to a Hedgehog

pathway inhibitor in medulloblastoma. Science *326*, 572–574. https://doi.org/10.1126/science.1179386.

103. Dobin, A., Davis, C.A., Schlesinger, F., Drenkow, J., Zaleski, C., Jha, S., Batut, P., Chaisson, M., and Gingeras, T.R. (2013). STAR: ultrafast universal RNA-seq aligner. Bioinformatics *29*, 15–21. https://doi.org/10.1093/bioinformatics/bts635.

104. Butler, A., Hoffman, P., Smibert, P., Papalexi, E., and Satija, R. (2018). Integrating single-cell transcriptomic data across different conditions, technologies, and species. Nat. Biotechnol. *36*, 411–420. https://doi.org/10.1038/nbt.4096.

105. McGinnis, C.S., Murrow, L.M., and Gartner, Z.J. (2019). DoubletFinder: Doublet Detection in Single-Cell RNA Sequencing Data Using Artificial Nearest Neighbors. Cell Syst. *8*, 329–337.e4. https://doi.org/10.1016/j.cels.2019.03.003.

106. Korsunsky, I., Millard, N., Fan, J., Slowikowski, K., Zhang, F., Wei, K., Baglaenko, Y., Brenner, M., Loh, P.R., and Raychaudhuri, S. (2019). Fast, sensitive and accurate integration of single-cell data with Harmony. Nat. Methods *16*, 1289–1296. https://doi.org/10.1038/s41592-019-0619-0.

107. Love, M.I., Huber, W., and Anders, S. (2014). Moderated estimation of fold change and dispersion for RNA-seq data with DESeq2. Genome Biol. *15*, 550. https://doi.org/10.1186/s13059-014-0550-8.

108. Yu, G., Wang, L.G., Han, Y., and He, Q.Y. (2012). clusterProfiler: an R package for comparing biological themes among gene clusters. OMICS *16*, 284–287. https://doi.org/10.1089/omi.2011.0118.

109. Liberzon, A., Birger, C., Thorvaldsdóttir, H., Ghandi, M., Mesirov, J.P., and Tamayo, P. (2015). The Molecular Signatures Database (MSigDB) hallmark gene set collection. Cell Syst. *1*, 417–425. https://doi.org/10.1016/j.cels.2015.12.004.

110. Shannon, P., Markiel, A., Ozier, O., Baliga, N.S., Wang, J.T., Ramage, D., Amin, N., Schwikowski, B., and Ideker, T. (2003). Cytoscape: a software environment for integrated models of biomolecular interaction networks. Genome Res. *13*, 2498–2504. https://doi.org/10.1101/gr.1239303.

111. Xiao, Z., Zou, Q., Liu, Y., and Yang, X. (2016). Genome-wide assessment of differential translations with ribosome profiling data. Nat. Commun. *7*, 11194. https://doi.org/10.1038/ncomms11194.

112. Wang, X., Li, Y., Wu, Z., Wang, H., Tan, H., and Peng, J. (2014). JUMP: a tag-based database search tool for peptide identification with high sensitivity and accuracy. Mol. Cell. Proteomics *13*, 3663–3673. https://doi.org/10.1074/mcp.O114.039586.

113. Aryee, M.J., Jaffe, A.E., Corrada-Bravo, H., Ladd-Acosta, C., Feinberg, A.P., Hansen, K.D., and Irizarry, R.A. (2014). Minfi: a flexible and comprehensive Bioconductor package for the analysis of Infinium DNA methylation microarrays. Bioinformatics *30*, 1363–1369. https://doi.org/10.1093/bioinformatics/btu049.

114. Zhou, W., Triche, T.J., Jr., Laird, P.W., and Shen, H. (2018). SeSAMe: reducing artifactual detection of DNA methylation by Infinium BeadChips in genomic deletions. Nucleic Acids Res. *46*, e123. https://doi.org/10.1093/nar/gky691.

115. McKenna, A., Hanna, M., Banks, E., Sivachenko, A., Cibulskis, K., Kernytsky, A., Garimella, K., Altshuler, D., Gabriel, S., Daly, M., and DePristo, M.A. (2010). The Genome Analysis Toolkit: a MapReduce framework for analyzing next-generation DNA sequencing data. Genome Res. *20*, 1297–1303. https://doi.org/10.1101/gr.107524.110.

116. Ritchie, M.E., Phipson, B., Wu, D., Hu, Y., Law, C.W., Shi, W., and Smyth, G.K. (2015). limma powers differential expression analyses for RNA-sequencing and microarray studies. Nucleic Acids Res. *43*, e47. https://doi.org/10.1093/nar/gkv007.

117. Narina, S., Connelly, J.P., and Pruett-Miller, S.M. (2023). High-Throughput Analysis of CRISPR-Cas9 Editing Outcomes in Cell and Animal Models Using CRIS.py. Methods Mol. Biol. *2631*, 155–182. https://doi.org/10.1007/978-1-0716-2990-1_6.

118. Connelly, J.P., and Pruett-Miller, S.M. (2019). CRIS.py: A Versatile and High-throughput Analysis Program for CRISPR-based Genome Editing. Sci. Rep. *9*, 4194. https://doi.org/10.1038/s41598-019-40896-w.

119. Endersby, R., Whitehouse, J., Pribnow, A., Kuchibhotla, M., Hii, H., Carline, B., Gande, S., Stripay, J., Ancliffe, M., Howlett, M., et al. (2021). Small-molecule screen reveals synergy of cell cycle checkpoint kinase inhibitors with DNA-damaging chemotherapies in medulloblastoma. Sci. Transl. Med. *13*, eaba7401. https://doi.org/10.1126/scitranslmed.aba7401.

120. Ong, T., Trivedi, N., Wakefield, R., Frase, S., and Solecki, D.J. (2020). Siah2 integrates mitogenic and extracellular matrix signals linking neuronal progenitor ciliogenesis with germinal zone occupancy. Nat. Commun. *11*, 5312. https://doi.org/10.1038/s41467-020-19063-7.

121. Weber, T.S., Jaehnert, I., Schichor, C., Or-Guil, M., and Carneiro, J. (2014). Quantifying the length and variance of the eukaryotic cell cycle phases by a stochastic model and dual nucleoside pulse labelling. PLoS Comput. Biol. *10*, e1003616. https://doi.org/10.1371/journal.pcbi.1003616.

122. Schwab, R.A.V., and Niedzwiedz, W. (2011). Visualization of DNA replication in the vertebrate model system DT40 using the DNA fiber technique. J. Vis. Exp. *e3255*, e3255. https://doi.org/10.3791/3255.

123. Lavado, A., Park, J.Y., Pare, J., Finkelstein, D., Pan, H., Xu, B., Fan, Y., Kumar, R.P., Neale, G., Kwak, Y.D., et al. (2018). The Hippo Pathway Prevents YAP/TAZ-Driven Hypertranscription and Controls Neural Progenitor Number. Dev. Cell *47*, 576–591.e8. https://doi.org/10.1016/j.devcel.2018.09.021.

124. Mercado-Ayon, E., Warren, N., Halawani, S., Rodden, L.N., Ngaba, L., Dong, Y.N., Chang, J.C., Fonck, C., Mavilio, F., Lynch, D.R., and Lin, H. (2022). Cerebellar Pathology in an Inducible Mouse Model of Friedreich Ataxia. Front. Neurosci. *16*, 819569. https://doi.org/10.3389/fnins.2022.819569.

125. Bankhead, P., Loughrey, M.B., Fernández, J.A., Dombrowski, Y., McArt, D.G., Dunne, P.D., McQuaid, S., Gray, R.T., Murray, L.J., Coleman, H.G., et al. (2017). QuPath: Open source software for digital pathology image analysis. Sci. Rep. *7*, 16878. https://doi.org/10.1038/s41598-017-17204-5.

126. Berg, S., Kutra, D., Kroeger, T., Straehle, C.N., Kausler, B.X., Haubold, C., Schiegg, M., Ales, J., Beier, T., Rudy, M., et al. (2019). ilastik: interactive machine learning for (bio)image analysis. Nat. Methods *16*, 1226–1232. https://doi.org/10.1038/s41592-019-0582-9.

127. Seimetz, J., Arif, W., Bangru, S., Hernaez, M., and Kalsotra, A. (2019). Cell-type specific polysome profiling from mammalian tissues. Methods *155*, 131–139. https://doi.org/10.1016/j.ymeth.2018.11.015.

128. Kojic, M., Gawda, T., Gaik, M., Begg, A., Salerno-Kochan, A., Kurniawan, N.D., Jones, A., Drożdżyk, K., Kościelniak, A., Chramiec-Głąbik, A., et al. (2021). Elp2 mutations perturb the epitranscriptome and lead to a complex neurodevelopmental phenotype. Nat. Commun. *12*, 2678. https://doi.org/10.1038/s41467-021-22888-5.

129. Su, D., Chan, C.T.Y., Gu, C., Lim, K.S., Chionh, Y.H., McBee, M.E., Russell, B.S., Babu, I.R., Begley, T.J., and Dedon, P.C. (2014). Quantitative analysis of ribonucleoside modifications in tRNA by HPLC-coupled mass spectrometry. Nat. Protoc. *9*, 828–841. https://doi.org/10.1038/nprot.2014.047.

130. Bai, B., Tan, H., and Peng, J. (2017). Quantitative Phosphoproteomic Analysis of Brain Tissues. Methods Mol. Biol. *1598*, 199–211. https://doi.org/10.1007/978-1-4939-6952-4_8.

131. Pagala, V.R., High, A.A., Wang, X., Tan, H., Kodali, K., Mishra, A., Kavdia, K., Xu, Y., Wu, Z., and Peng, J. (2015). Quantitative protein analysis by mass spectrometry. Methods Mol. Biol. *1278*, 281–305. https://doi.org/10.1007/978-1-4939-2425-7_17.

132. Xu, P., Duong, D.M., Seyfried, N.T., Cheng, D., Xie, Y., Robert, J., Rush, J., Hochstrasser, M., Finley, D., and Peng, J. (2009). Quantitative proteomics reveals the function of unconventional ubiquitin chains in proteasomal degradation. Cell *137*, 133–145. https://doi.org/10.1016/j.cell.2009.01.041.

133. Smith, K.S., Bihannic, L., Gudenas, B.L., Haldipur, P., Tao, R., Gao, Q., Li, Y., Aldinger, K.A., Iskusnykh, I.Y., Chizhikov, V.V., et al. (2022). Unified rhombic lip origins of group 3 and group 4 medulloblastoma. Nature *609*, 1012–1020. https://doi.org/10.1038/s41586-022-05208-9.

134. Liberzon, A., Subramanian, A., Pinchback, R., Thorvaldsdóttir, H., Tamayo, P., and Mesirov, J.P. (2011). Molecular signatures database (MSigDB) 3.0. Bioinformatics *27*, 1739–1740. https://doi.org/10.1093/bioinformatics/btr260.

135. Subramanian, A., Tamayo, P., Mootha, V.K., Mukherjee, S., Ebert, B.L., Gillette, M.A., Paulovich, A., Pomeroy, S.L., Golub, T.R., Lander, E.S., and Mesirov, J.P. (2005). Gene set enrichment analysis: a knowledge-based approach for interpreting genome-wide expression profiles. Proc. Natl. Acad. Sci. USA *102*, 15545–15550. https://doi.org/10.1073/pnas.0506580102.

136. Rapino, F., Delaunay, S., Rambow, F., Zhou, Z., Tharun, L., De Tullio, P., Sin, O., Shostak, K., Schmitz, S., Piepers, J., et al. (2018). Codon-specific translation reprogramming promotes resistance to targeted therapy. Nature *558*, 605–609. https://doi.org/10.1038/s41586-018-0243-7.

STAR★METHODS

KEY RESOURCES TABLE

REAGENT or RESOURCE	SOURCE	IDENTIFIER
Antibodies		
NEUN	Abcam	Cat#ab177487; RRID: AB_2532109
NEUN	Cell Signaling Technologies	Cat#24307; RRID: AB_2651140
BrdU	Abam-	Cat#ab6326; RRID: AB_2313786
PAX6	ThermoFisher Scientific	Cat#42-6600; RRID: AB_2533534
PAX6	BioLegend	Cat#901301; RRID: AB_2565003
PAX6	Abcam	Cat#ab195045; RRID: AB_2750924
γH2AX	Cell Signaling Technologies	Cat#9718; RRID: AB_2118009
RAD51	Abcam	Cat#ab133534; RRID: AB_2722613
53BP1	Novus Biologicals	Cat#NB100-304; RRID: AB_350221
53BP1	ThermoFisher Scientific	Cat#A300-272A; RRID: AB_185520
PRA32	Abcam	Cat#ab76420; RRID: AB_1524336
Cleaved Caspase-3	Cell Signaling Technologies	Cat#9664; RRID: AB_2070042
p53	Cell Signaling Technologies	Cat#2524; RRID: AB_331743
p-p53(S15)	Cell Signaling Technologies	Cat#9284; RRID: AB_331464
p53	Leica Biosystems	Cat#NCL-L-p53-CM5p; RRID: AB_2895247
p21	Abcam	Cat#ab109199; RRID: AB_10861551
p27	Invitrogen	Cat#MA5-33129; RRID: AB_2811945
p27	Invitrogen	Cat#PA5-27188; RRID: AB _2544664
ELP1	Millipore-Sigma	Cat#09-871; RRID: AB_10846498
ELP1	CUSABIO	Cat#CSB-PA011571LA01HU
ELP2	GeneTex	Cat#GTX121449; RRID: AB_10731459
ELP3	Cell Signaling Technologies	Cat#5728; RRID: AB_11178379
p27	Invitrogen	Cat#PA5-27188; RRID: AB_254464
Ki67	Abcam	Cat#Ab15580; RRID: AB_443209
Ki67	ThermoFisher Scientific	Cat#RM-9106; RRID: AB_2341197
MCM2	Abcam	Cat#ab4461; RRID: AB_304470
CDK2	Abcam	Cat#ab32147; RRID: AB_726775
p-CDK2	Cell Signaling Technologies	Cat#2561S; RRID: AB_2078685
Calbindin	Swant	Cat#300; RRID: AB_10000347
Calbindin	Cell Signaling Technologies	Cat#2173; RRID: AB_2183553
MDM2	Invitrogen	Cat#700555; RRID: AB_2532328
YAP1	Cell Signaling Technologies	Cat#14074; RRID: AB_2650491
YAP1	Santa Cruz	Cat#sc-101199; RRID: AB_1131430
GAB1	Santa Cruz	Cat#sc-133191; RRID: AB_2107855
β-catenin	Abcam	Cat#ab224803
β-catenin	Roche Diagnostics	Cat#760-4242; RRID: AB_2861317
RPS27a	Invitrogen	Cat#PA5-96039; RRID: AB_2807841
BrdU	BD Biosciences	Cat#347580; RRID: AB_10015219
BrdU	Abcam	Cat#AB6326; RRID: AB_305426
Anti-rabbit IgG, HRP-linked	Cell Signaling Technologies	Cat#7074; RRID: AB_2099233
Anti-mouse IgG, HRP-linked	Cell Signaling Technologies	Cat#7076; RRID: AB_330924

(*Continued on next page*)

Continued

REAGENT or RESOURCE	SOURCE	IDENTIFIER
Anti-Rabbit IgG (H + L) Crossed-absorbed, Alexa Fluor™ 594	ThermoFisher Scientific	Cat#A-11012; RRID: AB_2534079
Anti-Rabbit IgG (H + L) Crossed-absorbed, Alexa Fluor™ 488	ThermoFisher Scientific	Cat#A-11008; RRID: AB_143165
Anti-mouse IgG (H + L) Crossed-absorbed, Alexa Fluor™ 594	ThermoFisher Scientific	Cat#A-11005; RRID: AB_2534073
Anti-mouse IgG (H + L) Crossed-absorbed, Alexa Fluor™ 488	ThermoFisher Scientific	Cat#A-11001; RRID: AB_2534069
Chemicals, peptides, and recombinant proteins		
Neural Tissue Dissociation Kit (P)	Miltenyi Biotec	Cat#130-092-628
NE-PER™ Nuclear and Cytoplasmic Extraction Reagents	ThermoFisher Scientific	Cat#78835
AR6 Buffer	Akoya Biosciences	Cat# AR600250ML
AR9 Buffer	Akoya Biosciences	Cat# AR900250ML
ImmPRESS® Excel Amplified Polymer Staining Kit, Anti-Rabbit IgG, Peroxidase	Vector Laboratories	Cat#MP-7601
ImmPRESS® Excel Amplified Polymer Staining Kit, Anti-Mouse IgG, Peroxidase	Vector Laboratories	Cat#MP-7602
Invitrogen™ Click-iT™ EdU Cell Proliferation Kit, Alexa Fluor™ 488 dye	Invitrogen	Cat#C10337
Click-iT™ EdU Cell Proliferation Kit for Imaging, Alexa Fluor™ 594 dye	Invitrogen	Cat#C10339
Protein Normalization Module	Bio-techne	Cat#DM-PN02
Anti-Rabbit Detection Module	Bio-techne	Cat#DM-001
Anti-Mouse Detection Module	Bio-techne	Cat#DM-002
EZ Standard Pack 1	Bio-techne	Cat#PS-ST01EZ-8
EZ Standard Pack 5	Bio-techne	Cat# PS-ST05EZ-8
66-440 kDa Separation Module	Bio-techne	Cat#SM-W008
12-230 kDa Separation Module	Bio-techne	Cat#SM-W001
2-40 kDa Separation Module	Bio-techne	Cat#SM-W009
Pierce™ BCA Protein Assay Kit	ThermoFisher Scientific	Cat#23227
SuperSignal™ West Atto Ultimate Sensitivity Substrate	ThermoFisher Scientific	Cat#A38556
SuperSignal™ West Pico PLUS Chemiluminescent Substrate	ThermoFisher Scientific	Cat#34580
SuperSignal™ West Dura Extended Duration Substrate	ThermoFisher Scientific	Cat#34076
Allprep DNA/RNA Mini Kit	QIAGEN	Cat#80204
Cell Titer-Glo Luminescent Cell Viability Assay 2.0	Promega	Cat#G9241
Oligonucleotides		
Elp1-TATGACGTCCCCAGAGGCGG	SJCRH (CAGE)	SS151.Ikbkap.g17
Ptch1-GAGATCTCAGAGCGTGGCT	SJCRH (CAGE)	SS143.Ptch1.g31
Ptch1-GCATAGTGATATGGGTTTCG	SJCRH (CAGE)	SS143.Ptch1.g41
HDM2-AGACACTTATACTATGA	SJCRH (CAGE)	CAGE1980.HDM2.g2
HDM2-AACTTCAAAAGCAATGGCTT	SJCRH (CAGE)	CAGE1980.HDM2.g4
TP53-TCCTCAGCATCTTATCCGAG	SJCRH (CAGE)	RL9.TP53.g1
Experimental models: cell lines		
MED1712FH	Seattle Children's Hospital	Brain Tumor Research Laboratory
MED113FH	Seattle Children's Hospital	Brain Tumor Research Laboratory
RCMB24	Columbia University	Robert J. Wechsler-Reya

(*Continued on next page*)

Continued

REAGENT or RESOURCE	SOURCE	IDENTIFIER
SJMBSHH-13-5634	SJCRH	Martine F. Roussel
SJMBSHH-14-7196	SJCRH	Martine F. Roussel
Experimental models: organisms/strains		
Elp1$^{+/-16bp}$ mice (*Elp1*$_{HET}$)	SJCRH	Paul. A. Northcott
Elp1$_{WT}$;*Ptch1*$_{gRNA}$ tumors	SJCRH	Paul. A. Northcott
Elp1$_{HET}$;*Ptch1*$_{gRNA}$ tumors	SJCRH	Paul. A. Northcott
Elp1$_{gRNA}$;*Ptch1*$_{gRNA}$;*p53*$_{Null}$ tumors	SJCRH	Paul. A. Northcott
NSG mice (NOD.Cg-*Prkdc*^{scid}*Il2rg*^{tm1Wjl}/*SzJ*	The Jackson Laboratory	Strain #:005557
Nude mice (NU-*Foxn1*^{nu})	Charles River Laboratories	Strain #:088
Elp1$_{WT}$; *Atoh1-eGFP*	SJCRH	Paul. A. Northcott
Elp1$_{HET}$; *Atoh1-eGFP*	SJCRH	Paul. A. Northcott
CAS9-eGFP mice (*Gt(ROSA)26Sor*$^{tm1.1(CAG-cas9*,-EGFP)Fezh}$/J)	The Jackson Laboratory	Strain #:024858
Atoh1-eGFP mice (B6.129S-*Atoh1*$^{tm4.1Hzo/}$J)	The Jackson Laboratory	Strain #:013593
P53 null mice (B6.129S2-*Trp53*^{tm1Tyj}/J)	The Jackson Laboratory	Strain #:002101
Deposited data		
scRNA-seq, bulk RNA-seq,WGS, and DNA methylation array data	This paper	BioProject: PRJNA1083708
Expression data	This paper	GEO SuperSeries: GSE260851
Proteomic datasets from mouse tumors	This paper	Proteomics Identifications Database (PRIDE): PXD050487
Proteomic datasets from mouse GNPs	This paper	Proteomics Identifications Database (PRIDE): PXD050488
Software and algorithms		
BioRender	BioRender	
Prism	GraphPad	
ilastik v1.3	ilastik	
FlowJo™	BD Bioscience	
QuPath 4.0	Open Software for Bioimage Analysis	
Imaris (Bitplane)	Oxford Instrument	
STARsolo (v 2.7.1a)	Dobin et al.[103]	RRID:SCR_021542
Seurat (v4.1.0)	Butler et al.[104]	RRID:SCR_016341
DoubletFinder (v2.0.3)	McGinnis et al.[105]	RRID:SCR_018771
Harmony (v 0.1.0)	Korsunsky et al.[106]	RRID:SCR_022206
FastQC (v0.11.8)	https://www.bioinformatics.babraham.ac.uk/projects/fastqc	RRID:SCR_014583
BBDuk	https://jgi.doe.gov/data-and-tools/software-tools/bbtools/bb-tools-user-guide/bbduk-guide/	RRID:SCR_016969
STAR (v2.7.1a)	Dobin et al.[103]	RRID:SCR_004463
DESeq2 (v.1.42.0)	Love et al.[107]	RRID:SCR_015687
clusterProfiler (v.4.10.0)	Yu et al.[108]	RRID:SCR_016884
MSigDB (v7.4.1)	Liberzon et al.[109]	RRID:SCR_016863
Cytoscape (v3.10.1)	Shannon et al.[110]	https://cytoscape.org/
Xtail (v1.1.5)	Xiao et al.[111]	https://github.com/xryanglab/xtail
JUMP	Wang et al.[112]	https://github.com/JUMPSuite/JUMP
minfi (v1.44)	Aryee et al.[113]	RRID:SCR_012830
SeSAMe (v1.61)	Zhou et al.[114]	https://github.com/zwdzwd/sesame
GATK(v4.2)	McKenna et al.[115]	RRID:SCR_001876
limma (v3.54.2)	Ritchie et al.[116]	RRID:SCR_010943

EXPERIMENTAL MODEL AND STUDY PARTICIPANT DETAILS

Animal models

All experiments were conducted in accordance with the guidelines established by the National Institute of Health's Guide for the Care and Use of Laboratory Animals and approved by the St. Jude Children's Research Hospital (SJCRH) Institutional Animal Care and Use Committee (IACUC protocol #589–100536). Mice were housed with a 12-h light/dark cycle set with lights on from 6 a.m. to 6 p.m., with room temperature kept between 21°C and 23°C, and humidity between 30 and 80%. Temperature and humidity were continuously controlled and monitored. SJCRH is registered as a research facility with the USDA and maintains an assurance statement with the Office of Laboratory Animal Welfare of the NIH (Animal Assurance Number A3077-01).

NSG mice (NOD.Cg-*Prkdc*^{scid}*Il2rg*^{tm1Wjl}/*SzJ*, The Jackson Laboratory, JAX#005557) and Nude mice (NU-*Foxn1*^{nu}, Charles River Laboratories, Stock#088) were used as hosts for PDX implants. Female NSG/Nude mice at least 8 weeks of age were anesthetized in a surgical suite, and dissociated SHH-MB PDX cells were implanted in the cerebellum to expand tumor material for downstream analyses. Mice were observed daily and euthanized when reaching a humane endpoint.

Atoh1-GFP;*Elp1*$_{WT}$ or *Atoh1*-GFP;*Elp1*$_{HET}$ reporter mice were generated by cross breeding *Elp1*$_{HET}$ mice to *Atoh1*-GFP mice[47] (The Jackson Laboratory; B6.129S-*Atoh1*$^{tm4.1Hzo}$/J, JAX#103593). The *CAS9-eGFP* (The Jackson Laboratory; *Gt(ROSA)26Sor*$^{tm1.1(CAG-cas9*,-EGFP)Fezh}$/J, JAX#024858) were used to isolate GNPs that were subjected to viral transduction to knockout *Ptch1*, later implanted in NSG mice for tumorigenicity studies.

Patient-derived xenograft lines

Patient-derived xenograft lines MED1712FH, RCMB24, MED113FH, SJMBSHH-13-5634, and SJMBSHH-14-7196[77,78] were used for drug studies and associated genetic validation. Cells were incubated at 37°C in a humidified atmosphere at 5% CO2. Clinical characteristics of all patient-derived xenograft lines used listed in Table S6.

METHOD DETAILS

Risk analysis of SHH-MB patient data

We estimated cumulative risks[34] of SHH-activated medulloblastoma based on age-stratified (0–4, 5–9, 10–14, 15–19 years) odds ratios,[18] age-stratified frequencies of SHH-activated medulloblastoma,[18] and age-stratified population incidences of medulloblastoma.[33] The prospective UK Biobank cohort (394,841 individuals)[35] was used to estimate the population prevalence of rare pathogenic germline variants in *ELP1* (1 in 1,084 individuals), *PTCH1* (1 in 3,284), *TP53* (1 in 3,401), and *SUFU* (1 in 40,881). Rare germline missense variants in *TP53* were included and classified as pathogenic using functional data from the NCI *TP53* database (tp53.isb-cgc.org). For all other MB risk genes, only pLoF variants were considered. Population prevalence estimates for *PTCH1*, *SUFU*, and *TP53* are consistent with previous reports.[36,37]

Generation of *Elp1*$_{HET}$ mice

The *Elp1*$_{HET}$ (*Elp1*$^{+/-}$, also known as *Ikbkap*$^{+/-}$) mouse model was created using *CRISPR/Cas9* technology and direct zygote microinjection. Briefly, a chemically modified sgRNA (SS151.mIkbkap.g17 -5′- UAUGACGUCCCCAGAGGCGG -3'; Synthego) was tested prior to embryo injection for activity in mouse N2A cells (ATCC) stably expressing *SpCas9* and assayed by targeted next generation sequencing (NGS) using primers SS151.mIkbkap.DS.F – 5′ GCGTATGCTTTGTGAAAGGTGAA – 3′ and SS151.mIkbkap.DS.R – 5′-TGTTTTAATGTCACACCCGGC-3′ as previously described.[117] Resulting NGS data was analyzed using CRIS.py.[118] At 3–4 weeks, female C57BL/6J mice (JAX#00064) were subject to superovulation through gonadotrophin injections before mating with C57BL/6J males. Fertilized zygotes were collected the following morning in M2 media, stripped of cumulus cells with hyaluronidase. Zygotes were microinjected into the cytoplasm with a mixture of *SpCas9* mRNA (Trilink, 50 ng/μL) and SS151.*Ikbkap*.g17 (25 ng/μL) diluted in IDTE (Tris-EDTA, pH 7.5) buffer. After 1–4 h culture in M16 media, injected zygotes were transferred into the oviducts of day 0.5 pseudo-pregnant fosters (7-10-week-old) CD-1 females mated to vasectomized CD-1 males from Charles River Laboratories). Pups were genotyped at 7–10 days, and knockout-positive animals were weaned at 21 days of age. These procedures were conducted at the Center for Advanced Genome Engineering at SJCRH.

Tumorigenicity studies

For Elp1$_{HET\ or\ WT}$*;Ptch1*$_{gRNA}$ MB models, GNPs were isolated from cerebella of P7 *Elp1*$^{+/-}$*;Cas9-eGFP* mice (*Gt(ROSA)26Sor*$^{tm1.1(CAG-cas9*,-EGFP)Fezh}$/*J*, JAX#024858) and cultured on Poly-D-Lysine coated dishes in Granule Cell Medium (GCM) (50 mL Neurobasal Medium containing 1X Penicillin/Streptomycin, 2 mM Glutamine, 4.5% D-(+)-Glucose, 1x SPITE Medium Supplement, 1X Oleic Acid Albumin/Linoleic Acid, 1x B27, 1x N-Acetyl Cysteine), and 1 μg/mL recombinant mouse Shh (PeproTech, Inc. Cat#100-45). Next day, the transduction was performed with lentivirus mix carrying guide RNA targeting *Ptch1* (gRNA-31 GAGATCTCAGAGCGTGGCT and gRNA-41 GCATAGTGATATGGGTTTCG). After 24 h, the GNPs were harvested from the dishes and suspended in ice-cold DPBS. NSG mice were injected orthotopically with 1 million cells and monitored for signs of tumor growth with biweekly MRI imaging. Mice were observed daily and euthanized when reaching a humane endpoint.

For *Elp1*$_{WT\ or\ gRNA}$;*Ptch1*$_{gRNA}$;p53$_{null}$ MB models, GNPs were isolated from cerebella of P7 *p53*$_{null}$ mice (*B6.129S2-Trp53*^{tm1Tyj}/*J*, JAX#002101) and subjected to the same procedures as described above, except that the virus carrying guide RNA targeting *Elp1* was also added for transduction to knockout both the alleles of *Elp1* (gRNA-17 TATGACGTCCCCAGAGG).

In vitro FDA approved drug library sensitivity screening

In vitro drug screening was performed using 91 FDA-approved compound libraries on 5 SHH-MB PDX lines MED1712FH, RCMB24, MED113FH, SJMBSHH-13-5634, SJMBSHH-14-7196.[77,78] RCMB24 was originated and shared by Dr. Robert J. Wechsler-Reya's laboratory at Columbia University. MED1712FH and MED113FH were purchased from Brain Tumor Research Laboratory at Seattle Children's Hospital (previously Fred Hutchinson). SJMBSHH-13-5634 and SJMBSHH-14-7196 were shared by Dr. Martine F. Roussel at SJCRH. NSG mice were used as hosts for PDX implants. Freshly resected PDX tumors were cut into small pieces and incubated for 30 min at 37 °C in papain solution (10 units/mL, Worthington, LS003126) containing N-acetyl-L-cysteine (160 μg/mL, Sigma-Aldrich, A9165) and DNase I (12 μg/mL, Sigma-Aldrich, DN25), dissociated to single cells by gentle pipetting. Red blood cells in the tumor cell suspension were removed by incubating in RBC Lysis buffer (Stem Cell labs # 07850) at 37°C for 2 min, followed by rinsing in DPBS-BSA (0.05%). Cells were filtered using a 40μm strainer, counted and viability assessed to be above 80%. Cells were plated at optimal cell density (1000–3000) cells/well in 384 well plates containing FDA-approved compounds libraries with DMSO as a negative control in Tumor Stem Cell Medium (TSCM) containing 50% Dulbecco's Modified Eagle Medium/Nutrient Mixture F12 (DMEM/F12) plus 50% Neurobasal-A Medium supplemented with B-27 supplement (without vitamin A), 2 mM glutamine, 1 mM Sodium Pyruvate, 100 μM non-essential amino acids (NEAA), 10 μM HEPES, 20 ng/mL basic fibroblast growth factor , and 20 ng/mL epidermal growth factor. After incubation for 72 h, cell viability was measured using CellTiter-Glo Luminescent Cell Viability Assay 2.0 (Promega). Raw values were converted to cell viability percentages, and data were analyzed using GraphPad PRISM software to generate dose-response curves and calculate IC50 values.[119]

In vitro drug treatment

The PDX cells dissociated from MED1712FH, RCMB24 and MED113FH implanted mice were cultured *in vitro* in TSCM and subjected to treatments with DMSO vehicle, idasanutlin, selinexor, and idasanutlin + selinexor for 6 or 72 h, respectively. For cell viability assays, cytotoxicity of the drug treatment was assessed by measuring ATP content using CellTiter-Glo Luminescent Cell Viability Assay 2.0 (Promega). Drug source plates contained 1000X concentrated drug stocks, which were serially diluted 1:3 in DMSO to generate a 10-point dose-response curves. On the day of treatment, 30 nL of each drug was transferred directly into a 384-well white-cell plate (Greiner Bio-one, Cat#781080) using an Echo 655T liquid handler (Beckman Coulter). Vehicle control (0.1% DMSO) and 20 mM staurosporine were included as controls. Immediately afterward, 30 μL of cell suspension in growth medium was added to each well. Fast-growing cells were plated at 3000 cells/30 μL/well, while slow-growing cells were plated at 6000 cells/30 μL/well. The cell plates were incubated for 72 h in a 37°C humidifier incubator with 5% CO_2. At the end of treatment, the cell plates were brought to room temperature before adding 25 μL CellTiter-Glo reagent mix. After gently mixing for 10 min, the luminescent signal was detected using an EnVision plate reader (PerkinElmer). Curve fitting and IC50 values were generated using a four-parameter non-linear regression.[77] Drug combination synergy was assessed using the Bivariate Response to Additive Interacting Doses (BRAID) model, with Kappa as an indicator of drug interactions.[85] Response surface plots depict measured survival in response to dose-response of each of the two drugs at a 1:1 combination in full color; the best fitting BRAID response surface is depicted in the background, with contours of this surface shown in black.

For probing p53-MDM2 pathways, the PDX cells were treated for 6 h, followed by nuclear and cytoplasmic isolation using NE-PER Nuclear and Cytoplasmic Extraction Reagents Kit (ThermoFisher Scientific, Cat#78833). The whole cell and nuclear lysates were subjected to western blot analysis using ProteinSimple Jess System.

In vivo preclinical drug trials

In vivo preclinical drug trials of RG7388/idasanutlin, either alone or combined with selinexor, were performed in *ELP1-mutant* MED1712FH and *ELP1-wildtype* MED113FH PDX models across two independent trials. In brief, PDX lines MED113FH or MED1712FH were implanted into the cerebellum of Nude mice (Charles River Laboratory, stock #088). Mice were imaged for bioluminescence every week for tumor signals. Mice were enrolled once the tumor signal reached 5 x 10^5 relative light unit (RLU) or greater. Enrolled mice were divided at random into drugs/vehicle arms. For the first trial, enrolled mice were divided into vehicle- and idasanutlin-treated arms. For the second trial, enrolled mice were divided into vehicle-, idasanutlin-, selinexor-, and idasanutlin + selinexor-treated arms. For idasanutlin treatment, each arm was treated 2 times per day for 5 days during the first week of enrollment. They then rested for 3 weeks and were treated with a second-round 2 times per day for five days during the fifth week of enrollment. The second trial replicated the initial trial with a third cycle of idasanutlin treatment starting on week 12. For selinexor treatment, each arm was treated once a week for 3 weeks and rested for 1 week for two consecutive cycles. For combinational treatment, each arm was treated for two concurrent cycles of both idasanutlin and selinexor. All mice were monitored daily, and their health status was reported by an independent core. Endpoints were determined by the core's unbiased assessment of the animal's health.[119]

In vitro competition assay

The PDXs were freshly dissociated after harvesting from implanted NSG mice. The dissociated tumor cells were grown on Matrigel coated dishes in TSCM media. The guide RNAs (gRNA) targeting genes of interest and non-targeting gRNAs (negative control) were

used for comparison. The tumor cells were transduced with lentivirus carrying the *Cas9* with guide-RNA and GFP as marker to approximately transduce ~40–50% cells. The transduced cells were analyzed by flow cytometry 4 days post-transduction to measure the baseline transduction efficiency (GFP^+ percentage). The cells were again analyzed by flow cytometry a week after baseline measurements (11 days post-transduction) to check the effects of targeted gene knockouts on the transduced population dynamics. In such competition assays, cells sustaining inhibition of genes required for tumor maintenance will be outcompeted by non-transduced cells over the course of the experimental time frame leading to decrease in GFP+ percentage.

In vivo competition assay

The PDXs were freshly dissociated after harvesting from implanted NSG mice. The dissociated tumor cells were grown on Matrigel coated dishes in TSCM media. The guide RNAs (gRNA) targeting genes of interest and non-targeting gRNAs (negative control) were used for comparison. The tumor cells were transduced with lentivirus carrying the *Cas9* and guide-RNA with GFP as marker to approximately transduce ~40–50% cells. Next day, the tumor cells were harvested, and 1.5 million cells implanted orthotopically in immunodeficient NSG mice. A few million cells from each transduction group were left in culture, harvested after 4 days post-transduction, and analyzed by flow cytometry to measure the baseline transduction efficiency (GFP^+ percentage). The implanted mice from different groups were sacrificed same day after most of the mice reached humane endpoint and tumors were harvested. The tumors were dissociated with DM as described earlier. The tumor cells were processed for flow cytometry-based quantification of GFP^+ cells.

GNP isolation from P7 mouse cerebella

GNPs were purified as previously described[120] with minor modifications. Briefly, P7 $Elp1_{WT}$ *and* $Elp1_{HET}$ cerebella were dissected, dispersed and triturated into a single-cell suspension using the Neural Tissue Dissociation Kit P (Miltenyi Biotec, Cat#130-092-628). GNPs were isolated by centrifugation over a discontinuous Percoll gradient, and the higher-density fraction, which contained 95% GNPs and 5% glia, was collected. The glial cells were depleted by plating these cells twice on Poly-D-lysine coated culture dishes, as they attach more firmly than the loosely bound GNPs. The GNPs were flushed and counted and used for downstream assays. The GNPs processed for immunostaining were cultured for 24 h (h) on Poly-D-Lysine coated dishes in GCM.

Pulse labeling of GNPs in cultures and *in vivo*

S and G2 cell cycle phase labeling: GNP cells were grown in GCM containing 10 μM BrdU for 1 h and 30 min (min). After, the media was removed and replaced with GCM containing 10 μM EdU for another 30 min. The cells were fixed and processed for staining. The cells positive for only $BrdU^+$ were designated to be in G2-phase, and the double-positive $BrdU^+$ EdU^+ GNPs in S-phase.

S and G0/G1 cell cycle phase labeling: GNP cells were grown in GCM containing 10 μM BrdU for 30 min and media was removed with regular GCM for another 24 h. After 24 h, regular media was removed, and GNPs were incubated with GCM containing 10 μM EdU for 30 min.

S-phase labeling: The mice were intraperitoneally injected with EdU at a dose of 100 mg/kg and sacrificed 30 min later. The cells positive for EdU were designated as S-phase cells.

Cell cycle dynamics analysis using dual EdU/BrdU labeling

Cell cycle dynamic analysis using dual EdU/BrdU labeling was performed as previously reported[121] with some modifications. Briefly, GNP cultures were first exposed for 30 min windows to EdU (10μM), and 2 h afterward to BrdU (10μM) pulse for 30 min. After every pulse, we removed the analogs by replacing the medium; the nucleotide analogues are selectively incorporated into the DNA of GNPs that are actively replicating their genome (S-Phase) during these 30 min windows. At 2 h, 4 h, 6 h, and 8 h post-labelling, GNPs are collected and subjected to FACS. Our approach allowed the tracking of labeled GNP populations over time and the calculation of cellular proportions that transitioned from S to G2/M and later to the G0/G1 phase. A small population of labeled GNPs (EdU^+ or $BrdU^+$) transitioning from S to G0/G1 phases are located above G0-G1 population since they have divided and become diploid (2n by DAPI staining). To differentiate this population from EdU^- or $BrdU^-$ G0-G1 population, we named them G0*-G1*. All the flow cytometry analysis was performed on a FACS Aria Fusion (Becton Dickinson) using the 405nm laser to excite DAPI for cell cycle (450/50 bandpass filter), the 488nm laser for Alexa 488, (530/30 bandpass filter), and the 633nm laser for Alexa 647, (670/30 bandpass filter). The analysis of data post-acquisition was performed on both BD FACSDiva 8.01 and FlowJo software.

S-phase time length measurement

S-phase time length measurement was performed as previously described with some modifications.[54] GNPs were pulsed with 10 μM EdU for 2 h. After 2 h, the media was removed and fresh media containing 10 μM BrdU was added and cells incubated for another 30 min. Cells were fixed in 4% PFA and stained with anti-BrdU antibody (Abcam, Cat#ab6326). We calculated the S phase length according to the formula $Ts = Ti \times S$ cells/L cells. The percentage of cells in the S phase was calculated by measuring the leave fraction, the fraction of cells that exit the S phase in a determined time window, where Ti represents the time (h) between pulses, L cells were EdU^+ and $BrdU^-$, while S cells were $BrdU^+$.

DNA fiber assay and image analysis

This assay was performed as described previously with some modifications.[122,123] The GNPs were freshly isolated and grown on Poly-D-lysine coated at a density of 5 x10^6 cells per well of 6 well plate. The GNPs were pulsed with 25 mM CldU for 20 min, washed with pre-warmed PBS and then pulsed with 125 mM IdU for 20 min. The media was removed and GNPs harvested with pipetting using ice-cold PBS. The cells were pelleted down by centrifuging at 400g for 5 min, removing PBS, and resuspending in ice-cold PBS at a concentration of 5x10^5/mL. 2 μL of the cell suspension was air-dried on a Fisherbrand Superfrost Plus Microscope Slide for 3 min and lysed in 200 mM Tris-HCl (pH 7.5), 50 mM EDTA and 0.5% SDS solution for 2 min. All the slides were tilted at a 15° angle to let the lysis buffer drop down to bottom under gravity and let the fibers spread, air-dried for 5 h, and treated with methanol/acetic acid (3:1) for 10 min and 2.5 M HCl for 80 min. IdU and CldU were detected using specific antibodies. Anti-mouse BrdU 1:25 (BD Biosciences, Cat#347580) was used to detect IdU and Anti-rat BrdU 1:250 (Abcam, Cat#AB6326) was used to detect CldU. DNA fibers were imaged using a Zeiss Airyscan 980 confocal microscope at 63X with a 2X optical zoom. For each genotype, 3 independent replicates each having GNPs pooled from 4 to 5 mice were analyzed. Entire slides were imaged using tilling feature of ZEN 3.1 Blue (Zeiss) edition. For DNA fork speed, the length of the IdU tracks next to CldU tracks was measured and divided by the IdU incubation time (20 min). DNA fork asymmetry is expressed as ratio of long IdU/short IdU. IODs correspond to eye-to-eye distances (expressed in kbp), as exemplified in Figure 2G.

Atoh1-GFP flow cytometry

P7 *Elp1*$_{WT}$ or $_{HET}$;*Atoh1*-GFP mouse cerebella were dissociated for 30 min in papain solution (10 u/mL), rinsed in Neurobasal medium and filtered using a 40 μm strainer. The cells were resuspended in PBS with 0.05% BSA. Cell concentration and viability was assessed using DAPI staining. The cells were diluted to a final concentration of 1x10^6 cells/mL and analyzed by flow cytometry to determine the percentage of the GFP$^+$ cell population.

Sister chromatid exchange analysis

Mouse GNPs were isolated and treated with 200 nM 5-ethynyl-2-deoxyuridine (EdU) in the GCM medium for 24 h. EdU was then washed out and replaced with GCM medium without EdU for an additional 24 h of culture. During the final 4 h of culture, colecemid was added to the medium to collectively block and synchronize cells in mitosis. Cells were then removed from culture using Accutase and pelleted by centrifugation. Cells were resuspended in 0.075 M KCl for 8 min followed by centrifugation, KCl solution was removed and replaced with Carnoy's fixative (3:1 methanol to glacial acetic acid) and allowed to stand at room temperature for at least 15 min. Cells were centrifuged again, and fixative was replaced with fresh fixative. Air dried slides were made and detection of EdU was done using iFluor 488 azide (provided in Abcam-Cat#ab219801, EdU proliferation kit following manufacturer's instructions). Cells were then counter stained with DAPI and mounted in Vectashield mounting medium and imaged by fluorescence microscopy. Sister chromatid exchanges were then scored in metaphase cells.

Immunostaining

The GNPs were fixed with 4% paraformaldehyde (PFA), washed 3 times with PBS and stored at 4°C or processed for permeabilization. The cells were permeabilized with TBSTX (TBS+0.25% Triton X-100) for 15 min. Cells were incubated with 1% BSA in TBST (TBS+0.1% Tween 20) for 30 min to block non-specific binding of the antibodies. Incubated cells in the diluted primary antibody in 1% BSA in TBST were placed in a humidified chamber for 1 h at room temperature or overnight at 4°C. Cells were washed three times with TBST (TBS+0.1% Tween 20), 5 min each wash. Cells were incubated with the secondary antibody diluted in 1% BSA + TBST for 1h at RT in the dark, followed by three washes with TBST for 5 min. Cells were incubated in 1 μg/mL DAPI for 1 min, washed with TBST, and mounted with a mounting medium.

For immunostaining, paraffin-embedded sections were deparaffined, rehydrated, antigen-retrieved in Antigen Unmasking Solution (AR6 Buffer, Akoya Biosciences, Cat# AR600250ML), boiled for 20 min, and then subject to the immunohistochemistry procedure. EdU was detected by Invitrogen Click-iT EdU Cell Proliferation Kit (ThermoFisher, Cat#10337, #10339) as per the manufacturer's instructions.

Histopathology and IHC studies on human and mouse SHH-MB

Human and mouse SHH-MB tumors were evaluated by histomorphology and immunohistochemistry using the clinical molecular subtyping panel of stains.[68] Human *ELP1* mutant vs. *ELP1* wildtype SHH MB and mouse *Elp1*$_{HET}$;*Ptch1*$_{gRNA}$ vs. *Elp1*$_{WT}$;*Ptch1*$_{gRNA}$ MB mutant tumors were evaluated for comparison. Mouse tumors were stained using antibodies to YAP1 (Cell Signaling, clone D8H1X, Cat#14074), GAB1 (Santa Cruz, Cat#SC-133191), and beta-catenin (Roche Diagnostics, Cat#760–4242; Abcam, Cat#ab224803). All immunohistochemistry was performed on 4-μm-thick formalin-fixed paraffin embedded sections using automated Ventana Benchmark or Leica Bond III machines with appropriate secondary reagents. Molecular subtyping for human MBs was performed using immunohistochemistry with YAP1 (Santa Cruz, Cat#SC-101199), GAB1 (Santa Cruz, Cat#SC-133191), and beta-catenin (Roche Diagnostics, Cat#760–4242) as previously described.[68] All images are 40× magnification.

Multiplex chromogen immunohistochemistry

Immunohistochemistry studies in postnatal mice were performed as previously reported[124] with some modifications. Briefly, *Elp1*$_{HET}$ mice and *Elp1*$_{WT}$ littermates at P10 were anesthetized with CO_2 and cardiac perfused with 10 mL of PBS, followed by 20 mL of PBS

containing 10% formalin. Mouse brains were excised and immersed overnight in 10% formalin, washed in PBS, dehydrated, cut into half in a sagittal orientation and embedded in paraffin. A series of sagittal brain sections (4μm-thick) were obtained from the Comparative Pathology Core Facility at SJCRH. Paraffin-embedded sections were deparaffined, rehydrated, antigen-retrieved in Antigen Unmasking Solution and then subject to the immunohistochemistry procedure. To label the proliferating GNPs in oEGL, the differentiating GNPs in iEGL and Purkinje neurons of mouse cerebellum, we utilized ImmPRESS Excel Amplified Polymer Staining Kit, Anti-Rabbit or Anti-Mouse IgG, Peroxidase (Vector Laboratories) to optimize and validate the IHC staining of Ki67, p27, and calbindin antibodies in mouse cerebellum sections. After optimization and validation, the triple staining of Ki67, p27 and calbindin using multiplex chromogen immunohistochemistry was conducted at the Comparative Pathology Core using automated Ventana BenchMark IHC Stainers (Roche Diagnostic). Ki67, p27, and calbindin immunoreactivities were revealed as purple, brown and green using Discovery Purple, p27 ChromoMap DAB, Discovery Green HRP substrates (Roche Diagnostic). The stained slides were scanned using a Zeiss AxioScan Z1 slide scanner (Carl Zeiss Microscopy). Images were acquired using a 20X/0.8 NA objective. The areas and width of Ki67-positive oEGL and p27-positive iEGL in mouse cerebellum were annotated using QuPathv0.4.3 and quantified blindly as reported.[125,126] Briefly, we used QuPath v0.4.3 to draw regions of interest to select the tissue regions for the analysis and used the supervised machine-learning based approach using ilasik v1.3 to segment the pixels positive for Ki67 and P27. We then calculate the ratio of total Ki67 positive pixels to total P27 positive pixels per image.

Image acquisition and analysis

The mice cerebella sections and GNPs grown on Poly-D-lysine coated CultureWell Removable Chambered Coverglass (Electron Microscopy Sciences Cat#70459-08) were imaged by using either Confocal or AiryScan microscopy. Confocal and AiryScan microscopy was conducted on a Zeiss LSM980 confocal microscope using an α Plan-Apochromat 63x/1.4 NA objective. Z stacks were acquired at a digital zoom of 1.7 using 405, 488, 543, and 633 laser lines. AiryScan processing was subsequently performed in Zen Blue 3.4 (Carl Zeiss Microscopy). Slides were scanned using a Zeiss AxioScan Z1 slide scanner (Carl Zeiss Microscopy). Images were acquired using a 20X/0.8 NA objective. Brightfield images were acquired on a Hitachi HV-F202SCL. Fluorescent images were acquired using appropriate LED light source with excitation/emission filters and captured on a Hammamatsu Orca Flash camera.

Confocal and processed AiryScan images were analyzed using Imaris (Bitplane). Positive stained cells were identified as being above a threshold and mean fluorescence intensity was captured for each cell. Tissue sections scanned via the slide scanner were annotated for the region of interest and analyzed using QuPath. The number of positive cells and the ratio of positive cells to total cells were calculated.

Nuclear fractionation and western blotting analysis

For nuclear fractionation, we isolated nuclei from frozen tissues of ∼20 mg of mouse tumors using Parse Nuclear Isolation Protocol (Parse Bioscience) and lysed the isolated nuclei using NE-PER Nuclear and Cytoplasmic Extraction Reagents (ThermoFisher Scientific, Cat#78833). Protein expression in the nuclear lysates and total lysates was assessed as previously reported.[124] The protein concentration was determined using a BCA Protein Assay kit (ThermoFisher Scientific, Cat#23225). 15 μg of protein lysates were subjected to 4–12% NuPAGE Gel for electrophoresis and transferred to nitrocellulose membranes. Membranes were blocked with 3% nonfat milk and incubated with primary antibody overnight at 4°C. Blots were then incubated with appropriate horseradish peroxidase, HRP-conjugated secondary antibodies (Cell Signaling) for 2h at RT and then washed; reaction bands were visualized using a SuperSignal West Atto Ultimate Sensitivity chemiluminescence (ECL) substrate (ThermoScientific). Each blot was then incubated with stripping buffer (2% SDS, 50 mM Tris, pH 6.8, and 100 mM β-mercaptoethanol) for 45 min at RT to remove the antibodies and reprobed for other proteins including GAPDH as internal controls. Reaction product levels were quantified by scanning densitometry and normalized by the levels of GAPDH using NIH ImageJ software.

We used JESS Simple Western system following the manufacturer's protocol with modifications only to the concentrations of lysate and primary antibody. To analyze lysates on the JESS Simple Western instrument (ProteinSimple, Bio-Techne, Minneapolis, MN, USA), samples were diluted to total protein concentrations of 400–1000 ng/μL in 1X fluorescent master mix (EZ standard pack I; ProteinSimple, Bio-Techne), and 3 μL was added per well. 10 μL of primary antibody against the target was used at optimal concentrations (ranging 1:10-1:250). 10 μL of anti-rabbit HRP (DM-001, ProteinSimple, Bio-Techne) or anti-rabbit HRP (DM-002, ProteinSimple, Bio-Techne) secondary from Detection Modules were used. Enhanced chemiluminescence (ECL) reagents (Luminol and Peroxide) were used according to the kit's instructions (Chemiluminescence Detection module; ProteinSimple, Bio-Techne). Depending on the molecular weight of the target protein, antibody dilution, washing buffer, plates and capillary cartridges used were derived either from the 2–40 kDa, 12–230 kDa or 66–440 kDa Separation Modules (ProteinSimple, Bio-Techne). To allow sequential detection of Total protein (DM-TP01, ProteinSimple, Bio-Techne) or house-keeping control proteins, a RePlex reagent kit (RP-001, ProteinSimple, Bio-Techne) was used. JESS Simple Western data were analyzed using Compass for Simple Western software. Images from the high dynamic range 4.0 were used for the analysis, and peaks were automatically detected. Both peak height and area were analyzed after normalizing with either total protein or loading control.

Polysome profiling

Polysome profiling was performed as previously reported[127] with some modifications. Briefly the GNPs were isolated, and cell pellet snap frozen in liquid N_2 (LN_2). The 1.5 mL Eppendorf tubes containing the GNP pellet was placed in the mortar super cooled under LN_2. 150 mL of 1X polysome lysis buffer-pH 7.5 (10 mM Tris-HCl pH 7.5, 100 mM KCl, 5 mM $MgCl_2$, 0.5% (w/v) sodium deoxycholate,

1% (v/v) Nonidet-P40, 10mM DTT, 100 μg/mL cycloheximide, 1 U/mL SUPERaseIn RNase Inhibitor, 1X protease inhibitor cocktail (EDTA-free) in RNAse-free deionized water). The frozen mix of cell pellet and lysis buffer was pulverized using a pre-chilled pestle. Eppendorf tubes were placed on ice to thaw and mixed with pipetting using a 200 mL tip. Samples were centrifuged at 2000×g for 5 min at 4°C to pellet nuclei and cell debris. Supernatant was transferred to a fresh tube and centrifuged at 12,000×g for 5 min at 4°C. 150 mL of the resulting supernatant was loaded onto the top of a 10–50% sucrose gradient in 4 mL Polypropylene ultracentrifuge tubes (Cat# 344062, Beckman Coulter Inc). The tubes were centrifuged in a SW60Ti rotor at 246,606×g (38,000 RPM) for 125 min with low acceleration and brakes off. All tubing was washed with RNase-free H_2O at 3 mL/min using a clean ultracentrifuge tube. The BioComp Piston Gradient Fractionator was used to fractionate and record absorbance of the samples, setting the baseline absorbance by 60% sucrose. The first material to come out was free RNA and protein, followed by the 40S, 60S, 80S monosome, and increasing polysome peaks. Fractions were collected into microcentrifuge tubes as they exit the reader for use in downstream applications. Once the last of the sample was collected, several additional milliliters of 60% sucrose were flown through the tubing to clean it out and set the baseline again for the next sample. RNA was extracted separately from monosomic, disomic and polysomic fractions using TRIzol Reagent (Life Technologies) and processed for RNA-sequencing.

tRNA modification analysis

GNP cells and tumor tissue samples were homogenized in a TRIzol reagent (Life Technologies) using tissue homogenizer (Bertin Technologies), followed by RNA extraction. Total RNA and tRNA extraction, tRNA hydrolysis and modification analysis were performed as previously described.[128] In short, total RNA was isolated with phenol followed by chloroform extraction and precipitation by ammonium acetate and ethanol. Total tRNA was isolated from polyacrylamide gel (20% PAGE (19:1), 8 M urea, Tris-borate-EDTA (TBE) in 8 M urea, TBE buffer) following PAGE electrophoresis. Hydrolysis of tRNA to ribonucleosides was performed as previously described.[129]

High-performance liquid chromatography (HPLC) coupled to mass spectrometry (MS) was performed using a Luna Omega 1.6 μm, Polar-C18 100 Å column (150 mm × 2.1 mm, Phenomenex, Australia). MS parameters were defined for the ribonucleosides using multiple injections of 0.1–1 ng of purified ncm^5U, mcm^5U and mcm^5s^2U nucleosides (gift from Sebastian Leidel, University of Bern, Switzerland) and commercially obtained m^7G (Santa Cruz Biotechnology). Retention times were determined based on analyzing the purified ribonucleosides (ncm^5U, mcm^5U, mcm^5s^2U and m^7G) using HPLC-MS and for m^1A based on previously published results.[18] Peak assignment and quantification were performed using MultiQuant-v2.1.1 (ABSciex) software. Pseudouridine (Ψ) was used to normalize the data. Statistical analysis was performed using Prism v9.4.0 (GraphPad) software. Number of replicates, statistical tests and statistically significant differences are indicated in figure legends.

Protein digestion and tandem-mass-tag (TMT) labeling

The analysis was performed with a previously optimized protocol.[130,131] For whole proteome profiling, quantified protein samples (300 μg in the lysis buffer with 8 M urea) for each TMT channel were proteolyzed with Lys-C (Wako, 1:100 w/w) at 21°C for 2 h, diluted by 4-fold to reduce urea to 2 M for the addition of trypsin (Promega, 1:50 w/w) to continue the digestion at 21°C overnight. The insoluble debris was kept in the lysates for the recovery of insoluble proteins. The digestion was terminated by the addition of 1% trifluoroacetic acid. After centrifugation, the supernatant was desalted with the Sep-Pak C18 cartridge (Waters) and then dried by Speedvac (ThermoFisher). Each sample was resuspended in 50 mM HEPES (pH 8.5) for TMT labeling and then mixed equally, followed by desalting for the subsequent fractionation. For the whole proteome analysis alone, 0.1 mg protein per sample was used.

Extensive two-dimensional liquid chromatography-tandem mass spectrometry (LC/LC-MS/MS)

The TMT labeled samples were fractionated by offline basic pH reverse phase LC, and each of these fractions was analyzed by the acidic pH reverse phase LC-MS/MS.[112,132] We performed a 160 min offline LC run at a flow rate of 400 μL per minute on an XBridge C18 column (3.5 μm particle size, 4.6 mm × 25 cm, Waters; buffer A: 10 mM ammonium formate, pH 8.0; buffer B: 95% acetonitrile, 10 mM ammonium formate, pH 8.0).[130] A total of 80 2-min fractions was collected. Every forty-first fraction was concatenated into 40 pooled fractions which were subsequently used for whole proteome TMT analysis.

In the acidic pH LC-MS/MS analysis, each fraction from basic pH LC was dried by a Speedvac and was run sequentially on a column (75 μm × 35 cm for the whole proteome, 50 μm × 30 cm for whole proteome, 1.9 μm C18 resin from Dr. Maisch GmbH, 65°C to reduce backpressure) interfaced with a Fusion MS (ThermoFisher) for the whole proteome where peptides were eluted by a 90 min gradient (buffer A: 0.2% formic acid, 5% DMSO; buffer B: buffer A plus 65% acetonitrile). MS settings included the MS1 scan (450–1600 m/z, 60,000 resolution, 1 x 106 AGC and 50 ms maximal ion time) and 20 data-dependent MS2 scans (fixed first mass of 120 m/z, 60,000 resolution, 1 x 10^5 AGC, 110 ms maximal ion time, HCD, 36% normalized collision energy, 1.0 m/z isolation window with 0.2 m/z offset, and 10 s dynamic exclusion).

10X genomics single-cell RNA-sequencing data generation

Single cells from developing mouse cerebellar tissue were processed using the microfluidics-based 10X Chromium protocol as previously described.[133] Quantification and quality checks for the libraries were performed using an Agilent Technologies high sensitivity DNA 1000 chip. Libraries were sequenced on a NovaSeq 6000 (Illumina).

10X genomics single-cell RNA-sequencing data processing and analysis

STARsolo (v 2.7.3a) was used for mapping (mouse reference genome, mm10), demultiplexing and quantification for single cell RNA-seq. The gene expression matrix was then processed and analyzed by Seurat workflow (v4.1.0). Cells with gene feature <400 or mitochondrial percentage >15% were filtered out. Doublets were detected by DoubletFinder (v 2.0.3) with auto-optimized parameter estimation. Samples from different batches were integrated by Harmony (v 0.1.0). Cell types were predicted by Seurat TransferData using the mouse cerebellum atlas used as Smith et al.[133] Cell cycle was defined by Seurat CellCycle Scoring. For dimension reduction and clustering, we used the top 50 principal components as input for Louvain graph-based clustering, setting the resolution parameter at 1.0. We used Uniform Manifold Approximation and Projection (UMAP) for visualization purposes. The AddModuleScore function in Seurat was used to quantify gene sets. To establish a significant threshold for gene set enrichment, we randomly generated 1,000 gene sets, each equal in size to the input gene set and scored them to create a permuted null distribution. The enrichment threshold was then defined as the 99th percentile of this distribution. This threshold was then subtracted from the enrichment scores for visualization so that all cells above zero represent enriched cells. We analyzed cell type population abundance by calculating the percentage representation of each cluster in the sample, followed by a comparison across mouse conditions. Differential population abundance between wild-type and mutant was tested by beta-binomial regression-based statistical model using cell count for each cluster as input.

Bulk RNA-seq and functional enrichment analysis

FastQC-v0.11.8 was used to perform quality control of the RNA-Seq reads. Remaining adapters and low-quality bases were removed by BBDuk with parameter minlen = 30 and keeping default for others. Raw FASTQs were aligned to the mouse genome (mm10) or human genome (hg38) using STAR (v2.7.1a) to generate gene count matrices. Differentially expressed genes were processed using DESeq2 (v.1.42.0). Functional enrichment by GSEA was conducted using R package clusterProfiler (v.4.10.0) based on the biological processes Gene Ontology (GO), hallmark and curated gene set definitions from MSigDB (v7.4.1).[134,135] Functional enrichment results were filtered for significance with FDR<0.05. GSEA results were visualized in Cytoscape (v3.10.1) with network edges defined by Jaccard distance between gene set pairs.

Polysome profiling data analysis

Polysome profiling data was processed by the same methods as described in bulk RNA-seq. Differential translation analysis was performed using tool Xtail (v1.1.5),[136] which compares expression changes between polysome-associated mRNA and total mRNA across conditions to identify translationally regulated genes. The analysis employs DESeq2 for statistical modeling, utilizing Negative Binomial distributions to estimate variances and means, and then assesses the statistical significance and magnitude of differential translation through probability distributions and Empirical Bayes shrinkage for dispersion estimation. Functional enrichment analysis was performed as described above.

Identification of proteins by database search with JUMP software

The computational processing of identification was performed with the JUMP search engine to improve the sensitivity and specificity.[112] In general, commercially available software includes two major categories of algorithms: pattern-based scoring (e.g., SEQUEST and MASCOT) and tag-based scoring (e.g., PEAKS). JUMP combines pattern scoring with *de novo* tag scoring, displaying significant improvement in peptide-spectrum match (PSM) scoring. In this study, JUMP was used to search MS/MS raw data against a composite target/decoy database to evaluate FDR. All original target protein sequences were reversed to generate a decoy database that was concatenated to the target database. FDR in the target database was estimated by the number of decoy matches (nd) and the number of target matches (nt), according to the equation (FDR = nd/nt), assuming mismatches in the target database were the same as in the decoy database. The protein database was generated by combining downloaded Swiss-Prot, TrEMBL, and UCSC databases and removing redundancy (human: 83,955 entries; mouse: 59,423 entries), followed by concatenation with a decoy database. Major parameters included precursor and product ion mass tolerance (±15 ppm), full trypticity, static mass shift for the TMT tags (+304.2071453) and carbamidomethyl modification of 57.02146 on cysteine and dynamic mass shift for Met oxidation (+15.99491), maximal missed cleavage ($n = 2$), and maximal modification sites ($n = 3$). Putative PSMs were filtered by mass accuracy and then grouped by precursor ion charge state and filtered by JUMP-based matching scores (Jscore and ΔJn) to reduce FDR below 1% for proteins during the whole proteome analysis. If one peptide could be generated from multiple homologous proteins, based on the rule of parsimony, the peptide was assigned to the canonical protein form in the manually curated Swiss-Prot database. If no canonical form was defined, the peptide was assigned to the protein with the highest PSM number.

TMT-based peptide/protein quantification by JUMP software suite

The analysis was performed in the following steps, as previously reported with modifications[112]: (i) extracting TMT reporter ion intensities of each PSM; (ii) correcting the raw intensities based on the isotopic distribution of each labeling reagent (e.g., TMT126 generates 91.8%, 7.9% and 0.3% of 126, 127, 128 m/z ions, respectively); (iii) excluding PSMs of very low intensities (e.g., minimum intensity of 1,000 and median intensity of 5,000); (iv) removing sample loading bias by normalization with the trimmed median intensity of all PSMs; (v) calculating the mean-centered intensities across samples (e.g., relative intensities between each sample and the

mean), (vi) summarizing protein relative intensities by averaging related PSMs; (vii) finally deriving protein absolute intensities by multiplying the relative intensities by the grand-mean of three most highly abundant PSMs. In addition, we also performed y1-ion based correction of TMT data.

Differential expression (DE) analysis of proteins and false discovery rate evaluation

Differential protein abundance analysis was performed using limma (v.3.54.2), fitting linear models (lmFit function), and computing moderated t-statistics with empirical Bayes statistics (eBayes function). *p* values were adjusted for multiple testing.

DNA methylation data processing and analysis

Data processing involved reading IDAT files using the minfi (v1.44) and SeSAMe (v1.61) packages, with normalization steps including quality masking, inferring Infinium I channel, dye bias correction, and PooBah adjustment to generate beta values for methylation levels. Methylation profiles from human central nervous system (CNS) tumors[67] were integrated with those from mouse tumors using the software Harmony (v0.1.0) function HarmonyMatrix[106] using the top 3,000 variable probes that are common to both human and mouse methylation arrays.

Whole genome sequencing (WGS) data processing and mutation calling

Whole Genome Sequencing (WGS) reads are aligned to the mouse reference genome (mm10) using the BWA-MEM algorithm. Duplicate reads, identified by Picard (v3.0) as originating from the same DNA fragment, are marked and excluded from variant discovery to minimize artifacts from misaligned reads or indels. Base Quality Score Recalibration (BQSR) is implemented using GATK (v4.2) BaseRecalibrator and ApplyBQSR tools to correct systematic errors in base quality scores. Somatic SNVs were detected using GATK Mutect2 with GNP as normal controls ($Elp1_{WT}$, $n = 2$; $Elp1_{HET}$, $n = 2$). Only bi-allelic SNVs with an allelic fraction (AF) $\geq$0.05, a depth (DP) $\geq$ 20, and a TLOD $\geq$5 were retained. Variants present in three or more samples were excluded as likely germline mutations or sequencing artifacts. Known mouse strain SNPs were removed using the Mouse Genomes Project SNP database (version 5, Wellcome Trust Sanger Institute; https://ftp.ebi.ac.uk/pub/databases/mousegenomes/REL-1505-SNPs_Indels/mgp.v5.merged.snps_all.dbSNP142.vcf.gz).

QUANTIFICATION AND STATISTICAL ANALYSIS

Quantification of IF and IHC images were analyzed by senior imaging scientists blind to genotype using Imaris, QuPath 4.0, and ilastik v1.3. Quantification of Western Blots was analyzed using Compass for Simple Western software and ImageJ software. Details are provided in the STAR Methods sections. Significance was determined by the Mann-Whitney U test, Wilcoxon test, two-sided *t* test, and Chi-square test. Survival comparisons were quantified using log rank Mantel-Cox test. Statistical significance was determined with $^{*}p < 0.05$, $^{**}p < 0.01$, $^{***}p < 0.001$, $^{****}p < 0.0001$ for significant findings and $p > 0.05$ for non-significant (n.s.) results. Adjustments for multiple comparisons were made using the Benjamini-Hochberg procedure to control the false discovery rate (FDR). The exact statistical tests employed are detailed in the figure legends or results section.